

Development and characterisation of gyrotron-based Dynamic Nuclear Polarisation and Electron Paramagnetic Resonance spectroscopy at 9 Tesla

THÈSE N° 8590 (2018)

PRÉSENTÉE LE 16 MAI 2018

À LA FACULTÉ DES SCIENCES DE BASE

LABORATOIRE DE PHYSIQUE DES MATÉRIAUX NANOSTRUCTURÉS

PROGRAMME DOCTORAL EN PHYSIQUE

ÉCOLE POLYTECHNIQUE FÉDÉRALE DE LAUSANNE

POUR L'OBTENTION DU GRADE DE DOCTEUR ÈS SCIENCES

PAR

Murari SOUNDARARAJAN

acceptée sur proposition du jury:

Prof. P. Ricci, président du jury
Prof. J.-Ph. Ansermet, directeur de thèse
Prof. S. Jannin, rapporteur
Prof. R. Stern, rapporteur
Dr S. Alberti, rapporteur



ÉCOLE POLYTECHNIQUE
FÉDÉRALE DE LAUSANNE

Suisse
2018

Acknowledgements

The various parts that went into this PhD thesis were by no means an individual effort and I would like to take this opportunity to thank, at the outset, the people whose help and support were invaluable to me during this journey.

First and foremost, I must thank my thesis advisor, Prof. Jean-Philippe Ansermet, for providing me with the opportunity to carry out my studies in EPFL and for supervising and mentoring me during my research. His never-ending enthusiasm and optimism were highly contagious, and I am grateful for his readiness and availability to answer questions and discuss problems in the lab.

I would like to thank Prof. Paolo Ricci, Dr. Stefano Alberti, Prof. Sami Jannin and Prof. Raivo Stern for their participation as members of my thesis jury, for reading through the pages that follow and offering their corrections to the text, and for their extremely helpful remarks and suggestions about my work.

I would like to thank Dongyoung Yoon, who guided me through my experiments and introduced me to the lab equipment that I used for the better part of these four years. Indeed, as the person who taught me the nuts and bolts of NMR spectroscopy, I am deeply indebted to him for his help. I would also like to thank Alexandros, Christian, Felix, Marcin, Mika and the other past and present members of the LPMN for the many insightful discussions - and occasional piece of lab equipment - that we shared. Our many interesting conversations and pizza-lunches at Banane were welcome diversions from the conundrums that we faced down together in the lab. I also thank Dr. Christophe Roussel for his ideas and suggestions about the project.

The contribution of our collaborators at the Swiss Plasma Centre, Dr. Stefano Alberti, Dr. Falk Braunmüller and Jérémy Genoud, to this thesis cannot be overstated. Having developed and characterised the gyrotron, and then having instructed us in its use, it is safe to say that this project could not have begun without their involvement. Likewise, Dr. Emile de Rijk and the rest of the team at SwissTo12 played an instrumental role in the development and construction of the setup and I would like to thank Emile and Dr. Alessandro Macor in particular for laying the groundwork for the gyrotron-DNP experiment.

This project being a newly developed and constantly evolving one, I would be very remiss in

Acknowledgements

not acknowledging the help of Gilles Grandjean and his team at the mechanical workshop. Adrien Grisendi and Luc Chevalley in particular constructed many of the more challenging parts of the setup, and Claude Amendola had a hand in almost every experiment that was performed. I thank José Grandjean and Philippe Cuanillon of the electrical workshop for their ready assistance with stubborn apparatus, and Philippe's invaluable role in setting up and maintaining the gyrotron. I would also like to thank Dr. François Patthey of the LNS for his advice and assistance with our vacuum and cryogenic equipment.

Of course, a PhD is not all fun and games. It is often necessary to endure the pressures of holidaymaking, the drudgery of an evening by the lake or even the harsh realities of a chocolate-ricotta cake, and I am glad to have had the company of my friends Ana, Bart, Daniel, Eleonora and Amrita in these endeavours. I am eternally grateful for their presence and support during these past six years in Lausanne, and I cannot thank them enough for the innumerable moments of happiness that we shared.

Finally, I would like to thank my family for all their encouragement and inspiration, and my parents in particular for nurturing my curiosity as a child and helping set me on the path that has led me here.

Lausanne, 20 April 2018

Murari Soundararajan

Abstract

The Dynamic nuclear polarisation (DNP) enhanced nuclear magnetic resonance (NMR) results presented in this thesis demonstrate the functionality of a tunable and switchable gyrotron operating at 260 GHz with a 9 T spectrometer. This gyrotron was designed at the Swiss Plasma Center. Millimeter wave passive components were built by the startup company SwissTo12. Monochromatic as well as frequency swept cross effect DNP experiments validate the basic functioning and frequency tunability of the gyrotron. High power operation is tested on systems exhibiting the Overhauser and solid effects with the aid of a novel planar probe designed to mitigate dielectric heating. Microwave polarisation control using a Matching Optics Unit is verified using cross effect DNP. Continuous wave electron paramagnetic resonance (EPR) measurements performed on a home built quasi-optical spectrometer operating at 260 GHz on the same sample space as the NMR spectrometer are also presented. EPR spectra of hyperpolarising agents measured on this spectrometer are used to prepare for and subsequently analyse the DNP experiments. Preliminary studies on surface modified titanium dioxide nanopowders using EPR at 9 GHz, displaying significant g-factor shifts are reported.

Keywords: DNP-NMR, Gyrotron based DNP, Hyperpolarisation, High-field EPR, Tunable gyrotrons, Titanium dioxide.

Résumé

Les résultats des expériences de résonance magnétique nucléaire (RMN) présentés dans cette thèse démontrent le fonctionnement d'un gyrotron, commutable et accordable en fréquence, conçu pour la polarisation dynamique nucléaire (DNP) à 260 GHz et 9 T. Des expériences de DNP réalisées par la méthode dite « cross effect », effectuées avec des micro-ondes monochromatiques ainsi que des micro-ondes balayées en fréquence, valident le fonctionnement du gyrotron en mode basique ou accordé en fréquence. Des points de fonctionnement à haute puissance sont testés avec des systèmes sujets à l'effet Overhauser et l'effet solide (« solid effect ») à l'aide d'une sonde novatrice de géométrie plane, conçue afin d'atténuer l'échauffement diélectrique. Le contrôle de la polarisation des micro-ondes est aussi vérifié par la DNP. La résonance paramagnétique électronique (RPE) en ondes continues mesurée en utilisant un spectromètre quasi-optique fait maison est également présentée. Ce spectromètre fonctionne à 260 GHz sur le même cryostat que le spectromètre à RMN. Les spectres RPE des agents d'hyperpolarisation pris avec ce spectromètre guident la préparation à l'expérience de DNP et fournissent des données qui contribuent à l'analyse des expériences DNP. Des études RPE préliminaires, à 9 GHz, sur des nanopoudres d'oxyde de titane à surface modifiée sont présentées, qui montrent des décalages de fréquence significatifs des rapports gyromagnétiques observés.

Mots clés : DNP-NMR, Gyrotron-DNP, Hyperpolarisation, RPE à haut champ, Gyrotrons accordables, Oxyde de titane.

Contents

Acknowledgements	iii
Abstract (English/Français)	v
List of figures	xi
List of tables	xiii
Introduction	1
1 Overview of DNP Mechanisms	5
1.1 Overhauser effect	5
1.1.1 Cross relaxation mechanisms	7
1.1.2 Electron spin saturation	7
1.2 Solid effect	10
1.3 Cross effect	11
2 DNP and EPR Instrumentation	15
2.1 DNP-NMR Spectrometer	15
2.1.1 Gyrotron source for high power 260 GHz radiation	15
2.1.2 Matching Optics Unit and polarisation control	18
2.1.3 Planar Probe	21
2.2 Martin-Pupplett EPR Spectrometer	22
3 DNP Results	29
3.1 Cross Effect DNP	29
3.1.1 Sample preparation	29
3.1.2 ^1H DNP	31
3.1.3 Microwave polarisation control	32
3.1.4 Frequency modulated DNP	34
3.1.5 Analysis of cross effect DNP	36
3.2 Solid Effect DNP	39
3.3 Overhauser Effect DNP	39
3.3.1 ^{31}P DNP in solution	40
3.3.2 ^1H DNP in solution	42

Contents

3.3.3	BDPA doped polystyrene	42
3.3.4	Analysis of Overhauser DNP	43
4	EPR Results	47
4.1	EPR of Hyperpolarising Agents	49
4.1.1	TEMPOL in frozen solution	49
4.1.2	BDPA	49
4.1.3	Diamond nanopowder	52
4.2	Paramagnetic Centres in Titanium Dioxide	54
4.3	Conducting Polymers	58
	Conclusion and Future Prospects	61
A	NMR of Functionalised TiO₂	65
A.1	Formic acid functionalised TiO ₂	65
A.2	Phosphoric acid functionalised TiO ₂	66
A.3	Cross effect ¹ H DNP on TiO ₂	68
B	Optically Pumped Hyperpolarisation in InP	69
	Bibliography	71
	Curriculum Vitae	77

List of Figures

1.1	Energy level diagram of two spins-1/2	5
1.2	Sketch of a Homogeneous EPR Line	8
1.3	Sketch of Expected Solid Effect Enhancement Profile	11
1.4	Sketch of Inhomogeneous EPR Line	12
2.1	Schematic of the DNP-NMR Setup	16
2.2	Tunability of the gyrotron	17
2.3	Rapid switching of the gyrotron output	17
2.4	Gyrotron operation during temperature jump DNP	18
2.5	The universal matching optics unit	19
2.6	Characterisation of microwave polarisation	20
2.7	The planar probe	22
2.8	Simulation of planar probe	23
2.9	Layout of the EPR spectrometer	24
2.10	Martin-Pupplett optical path	25
2.11	EPR spectrometer CAD drawing	26
2.12	EPR spectrometer photograph	26
2.13	EPR probehead	27
3.1	TEMPOL structure and EPR spectrum	30
3.2	Schematics of DNP pulse and trigger sequence	31
3.3	Cross effect enhancement as a function of temperature	32
3.4	Gyrotron enhancement map	33
3.5	Complete enhancement map	33
3.6	Enhancement as a function of polarisation	34
3.7	Frequency modulation profile	34
3.8	Enhancement with frequency modulation - VDI source	35
3.9	Raw data enhanced by frequency modulation	36
3.10	Enhancement with frequency modulation - gyrotron	37
3.11	Solid Effect DNP Enhancements	40
3.12	Liquid Overhauser DNP - TPP/BDPA	41
3.13	¹ H NMR and DNP spectrum in liquid water	42
3.14	Overhauser Effect in polystyrene	43

List of Figures

3.15 Overhauser Effect in an polystyrene	44
3.16 ^{31}P Overhauser DNP power dependence: fitting	44
4.1 Martin-Pupplett measurement procedure	48
4.2 TEMPOL frozen EPR spectrum	50
4.3 BDPA EPR spectra	51
4.4 BDPA in polystyrene EPR	52
4.5 Diamond EPR Spectra	53
4.6 Titania EPR Under UV Irradiation	55
4.7 Functionalised titania EPR under UV irradiation	56
4.8 Hydrogen Treated Titania	57
4.9 Polyaniline EPR spectra	59
A.1 NMR Spectrum of Formic Acid on Titania	66
A.2 NMR Spectrum of Phosphoric Acid on Titania	67
A.3 NMR Spectrum of Phosphoric Acid on Titania	67
A.4 DNP Measurement on Dehydrated TiO_2	68
B.1 OPNMR of Indium Phosphide	69

List of Tables

4.1 Diamond Simulation Parameters	54
---	----

Introduction

Nuclear Magnetic Resonance (NMR) is a very versatile tool that provides information about magnetic environment of specific nuclei or spins. This permits diverse uses such as magnetic resonance imaging (MRI), structure elucidation, studies of interfaces and molecular diffusion among others. However, the primary drawback of NMR is its low sensitivity - it is commonly acknowledged that the minimum number of nuclear spins measurable in a conventional room temperature NMR experiment at high field is 10^{17} . This is a direct result of the low magnetic moment of nuclei, due to the relatively large nuclear mass. In comparison, the magnetic moment of a free electron, with a mass three orders of magnitude smaller than that of a nucleus, is a factor of 658 times larger than that of ^1H , the most common isotope of hydrogen. This low sensitivity is compounded by the fact that NMR active isotopes of many important elements such as carbon and oxygen naturally only occur in trace quantities. Thus, it would be highly beneficial to develop techniques to combine the high sensitivity of Electron Paramagnetic Resonance (EPR) with the versatility of NMR. Dynamic Nuclear Polarisation (DNP) is one such technique, which transfers the magnetisation of paramagnetic electrons in a sample to a target nuclear species, temporarily increasing the sensitivity of NMR detection by several orders of magnitude. First proposed by Overhauser in 1953 for metals, in which nuclei are immersed in a bath of paramagnetic conduction electrons [1], DNP has since been observed in a variety of different systems including liquids. The four chief mechanisms proposed are the Overhauser Effect, the Solid Effect, the Cross Effect and Thermal Mixing. These mechanisms occur in highly specific conditions and samples under study often need to be tailored to favour DNP through a given mechanism, such as by doping with specialised paramagnetic impurities and free radicals. In some materials, such external hyperpolarising agents do not need to be added and DNP is feasible in the unmodified material itself. Such 'endogenous DNP' can be performed in alkali metals, in coal and other allotropes of carbon [2], and in certain protein molecules [3] among others.

DNP has been extensively used at 0.3 T (where the electron Larmor frequency of 9 GHz falls in the 'X-band' of the IEEE standard) in the liquid state in studies of water dynamics surrounding biomolecules [4, 5]. In the solid state, surface defects in silicon micro- and nanoparticles have been used to hyperpolarise the nuclei by the solid effect for use in in-vivo MRI [6, 7]. The technique of dissolution DNP, using the thermal mixing mechanism in frozen solutions of monoradicals at less than 2 K, was first introduced in 2003 by Ardenkjaer-Larsen et al at 3 T [8]

Introduction

and has been used ever since to obtain up to 40 % nuclear polarisation in liquid state NMR [9]. The advantages of high spectral resolution and increased sensitivity offered by high field NMR were explored using superconducting magnet systems that were commercially available by the 1970s. Extending the reach of DNP to these high fields, however, was a technological challenge that has only recently been overcome. Microwave transmission at the sub-terahertz frequencies required for high field DNP is quasi-optical by necessity, and the small sizes of microwave resonators precludes some experiments such as magic angle spinning (MAS). The use of gyrotrons as high power microwave sources for DNP was pioneered by the Griffin group at 5 T in 1995 [10] and at 9 T in 2003 [11].

The project that this thesis is a part of originated in 2008 as a collaboration at EPFL among our group, the Laboratory of Magnetic Resonance of Prof Bodenhausen and the Swiss Plasma Centre, to develop a home built flexible gyrotron system for DNP at 9 T. Previous research in the group and by others on NMR of high surface area catalysts, in particular, of gases such as carbon monoxide adsorbed on platinum and palladium yielded insights into molecular diffusion and the nature of the chemical bond between adsorbant and adsorbate [12–14]. Building upon this work, the ultimate goal of the project is to achieve DNP enhanced surface NMR in electrochemical and catalytic systems. The gyrotron, deployed in the LPMN towards the end of 2013, was one of the first frequency tunable and switchable gyrotrons designed for DNP. As the microwave power required for DNP can be rather high depending on the mechanism and experimental conditions, the gyrotron was designed to output a maximum of 100 W. In order to manage the heat generated by such high power irradiation, a planar probe was developed in collaboration with SwissTo12, with the additional advantage of having a geometry suitable for future electrochemistry experiments as well. Being an entirely home built spectrometer, extensive characterisation and testing was necessary, which makes up the bulk of this thesis. The now-standard cross effect DNP experiment in frozen solutions of nitroxide radicals was used as the initial test experiment, including optimisation of the glass forming mixture and radical composition. The planar probe's capabilities were tested using solid effect measurements and Overhauser experiments in liquids, as well as the newly reported Overhauser effect in insulating solids. In parallel with the gyrotron-DNP, a high field EPR spectrometer was developed in the group by Caspers et al [15], with a view to supplementing the DNP experiments. EPR measurements of the polarising agents in the same field and conditions as the DNP is desirable for both pinpointing the gyrotron frequency needed and for studying the systems and mechanisms in more detail. Characterisation of the EPR setup as well as measurements on systems used for DNP make up the remainder of this thesis.

Gyrotron based DNP has now become a standard commercial package for solid state MAS spectrometers, developed and sold by Bruker since 2008. The most common methods to achieve DNP in these systems involve mixing solid samples with solutions of specially tailored biradicals and making use of the cross effect at low temperatures. When this method is used to study surfaces, it is often referred to as Surface Enhanced NMR Spectroscopy (SENS). It has been used to study catalytic sites on the surface of heterogeneous catalysts such as

amorphous silica-alumina [16]. SENS has been useful in measuring natural abundance oxygen NMR to study the environments of hydroxyl groups on the surface of such catalysts [17] as well. DNP in static conditions has also been used to detect aluminium NMR signals on these samples [18] as well as to record ultra-wide linewidth NMR spectra, such as that of platinum in metal-organic frameworks [19]. Sensitivity gains of even one order of magnitude dramatically reduce experimental time in multi-dimensional NMR experiments, and such DNP enhanced measurements have been recently used for protein structure determination to very high resolution [20]. Homonuclear carbon-carbon correlation measurements at natural abundance of species loaded on mesoporous catalyst have also been recently reported, in an experiment that would be impractical without the sensitivity enhancement due to DNP [21].

1 Overview of DNP Mechanisms

The hyperpolarisation mechanisms used in the DNP experiments in this thesis - the Overhauser effect, the solid effect and the cross effect - have well established theoretical explanations, and this chapter will outline key points of these standard theories. All three mechanisms involve transfer of polarisation from electrons, here described by a spin-1/2 S , to a nuclear species, here assumed to be a spin-1/2 I for simplicity.

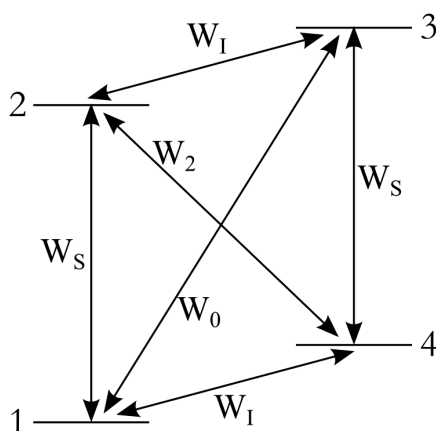


Figure 1.1 – A schematic energy level diagram of a system consisting of two weakly interacting spins-1/2. The transition rates between energy levels are represented as W

1.1 Overhauser effect

The level diagram for the system of spins-1/2 S and I discussed here is shown in figure 1.1. For a system of non-interacting spins, the only off-diagonal terms in the spin Hamiltonian are due to radio frequency and microwaves. Only the single quantum transitions (with rates W_I and W_S) are ‘allowed’ while the cross transitions are ‘forbidden’. The presence of hyperfine

Chapter 1. Overview of DNP Mechanisms

interaction between spins I and S introduces off-diagonal terms linking the electronic and nuclear subspaces, causing the zero and double quantum transitions to become ‘allowed’ as well. The Overhauser effect relies on saturation of the electronic single quantum transitions and cross-relaxation of the electrons and nuclei through the hyperfine interaction, thus resulting in polarisation transfer.

For the system in figure 1.1, the expectation values of the z-magnetisations of the nuclei and electrons can be expressed in terms of the populations of the energy levels as

$$\begin{aligned}\langle \hat{I}_z \rangle &= (n_1 + n_2) - (n_3 + n_4) \\ \langle \hat{S}_z \rangle &= (n_2 + n_3) - (n_4 + n_1)\end{aligned}$$

Using the transition rate constants W_I, W_S, W_0, W_2 , rate equations for the populations can be established, which imply for $d\langle \hat{I}_z \rangle / dt$ and $d\langle \hat{S}_z \rangle / dt$ the Solomon equations [22]

$$\begin{aligned}\frac{d\langle \hat{I}_z \rangle}{dt} &= -(2W_I + W_0 + W_2)(\langle \hat{I}_z \rangle - \langle \hat{I}_z^0 \rangle) - (W_2 - W_0)(\langle \hat{S}_z \rangle - \langle \hat{S}_z^0 \rangle) \\ \frac{d\langle \hat{S}_z \rangle}{dt} &= -(W_2 - W_0)(\langle \hat{I}_z \rangle - \langle \hat{I}_z^0 \rangle) - (2W_S + W_0 + W_2)(\langle \hat{S}_z \rangle - \langle \hat{S}_z^0 \rangle)\end{aligned}$$

where $\langle \hat{S}_z^0 \rangle$ and $\langle \hat{I}_z^0 \rangle$ are the thermal equilibrium expectation values.

In the steady state,

$$\langle \hat{I}_z \rangle = \langle \hat{I}_z^0 \rangle - \frac{W_2 - W_0}{2W_I + W_0 + W_2} (\langle \hat{S}_z \rangle - \langle \hat{S}_z^0 \rangle)$$

Rearranging the terms, we obtain an enhancement ϵ in nuclear polarisation of

$$\begin{aligned}\epsilon &= \frac{\langle \hat{I}_z \rangle - \langle \hat{I}_z^0 \rangle}{\langle \hat{I}_z^0 \rangle} = -\frac{\langle \hat{S}_z^0 \rangle}{\langle \hat{I}_z^0 \rangle} \frac{W_0 - W_2}{W_0 + W_2} \left(1 - \frac{2W_I}{2W_I + W_0 + W_2} \right) \left(1 - \frac{\langle \hat{S}_z \rangle}{\langle \hat{S}_z^0 \rangle} \right) \\ &= \frac{|\gamma_S|}{|\gamma_I|} \xi f s\end{aligned}$$

The coupling factor $\xi = (W_0 - W_2)/(W_0 + W_2)$ denotes the efficiency of the polarisation transfer. The leakage factor f describes nuclear relaxation through other competing processes and the saturation factor s describes the extent of electron spin depolarisation.

1.1.1 Cross relaxation mechanisms

The most general form of the hyperfine interaction Hamiltonian, which is responsible for cross-relaxation between electrons and nuclei, is due to the hyperfine tensor \mathcal{A} and has the form

$$\hat{\mathcal{H}}_{\text{hf}} = \hbar \hat{\mathbf{S}} \cdot \mathcal{A} \cdot \hat{\mathbf{I}}$$

While this expression includes all possible spin flip terms, it does not by itself provide the energy for any of these transitions to occur. However, other interactions such as molecular motion and electron spin-lattice relaxation can do so. These interactions are modelled as time variations in the hyperfine tensor and the electron spin, and can together be written as a time varying magnetic field $\mathbf{H}_e(t)$, and the Hamiltonian is now

$$\hat{\mathcal{H}}_{\text{hf}} = -\hbar \gamma_I \hat{\mathbf{I}} \cdot \mathbf{H}_e(t)$$

In this formulation, cross-relaxation can occur if the spectral density of $\mathbf{H}_e(t)$ has a significant value at ω_{0I} , satisfying the energy requirement for a nuclear spin flip. Following Abragam [23], this can be divided into two categories: one where the fluctuation in time of the hyperfine tensor, due to molecular motion or phonons, satisfies this condition, and the other where fluctuation in the electron spin due to T_1 relaxation processes does so. The hyperfine tensor can be purely scalar, in which case ξ is positive and has a maximum value of +1, purely dipolar, in which case ξ is negative with maximum value $-1/2$, or a mixture of the two. Cross-relaxation due to the first category, including metals and solutions of paramagnetic salts in liquids, can be due to either scalar or dipolar coupling. Scalar coupling results in a positive enhancement and can be seen in the BDPA - triphenyl phosphine system in, while dipolar coupling results in a negative enhancement such as in the TEMPOL - water system, both seen in section 3.3. According to Abragam, Overhauser DNP due to electron spin fluctuation, which includes insulating solids, can only be due to scalar coupling. While the BDPA PS system in section 3.3.3 shows positive enhancement indicating scalar coupling, more systems need to be studied to verify this prediction.

1.1.2 Electron spin saturation

The EPR lineshape for a species with an isotropic g tensor is not an infinitely sharp delta function at the Larmor frequency, but is broadened due to spin-spin relaxation. The functional form is in general a Lorentzian

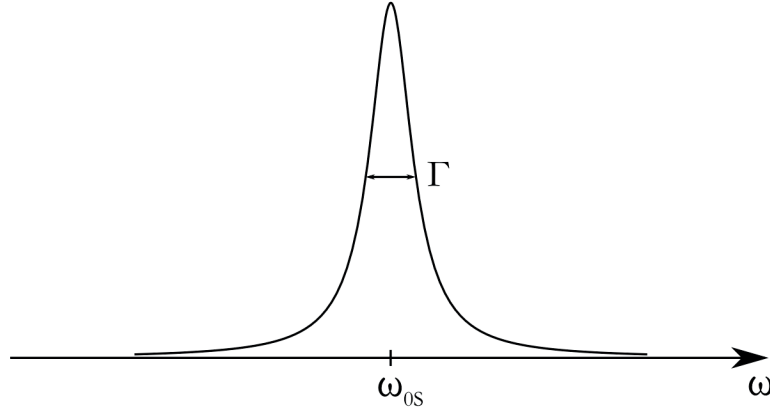


Figure 1.2 – Example of a homogeneous EPR line $h(\omega - \omega_{0S})$ centred at the electron Larmor frequency

$$h(\omega) = \frac{1}{\pi} \frac{\frac{1}{2}\Gamma}{\omega^2 + (\frac{1}{2}\Gamma)^2}$$

As the Overhauser effect relies purely on saturation of this EPR line, the microwave absorption and enhancement profiles will have the same Lorentzian shape, as shown in figure 1.2.

The electron spins are saturated by means of microwaves at or close to the electron Larmor frequency, ω_{0S} . The magnetic field due to linearly polarised microwaves takes the form $2B_1 \cos \omega_m t \mathbf{x}$, where $2B_1$ is the peak amplitude and $\omega_m = 2\pi f_m$ is the angular frequency of the microwaves. The electron spin Hamiltonian due to this and the external, static magnetic field B_0 is

$$\hat{\mathcal{H}}_S = \hbar \omega_{0S} \hat{S}_z + 2\hbar \omega_{1S} \cos \omega_m t \hat{S}_x$$

where $\omega_{\{0,1\}S} = -\gamma_S B_{0,1}$ are the electron Larmor frequencies due to the static and microwave magnetic fields. As it is more convenient to view the system in the rotating frame of the microwaves, this Hamiltonian is transformed into a frame rotating at the same angular frequency as the microwaves and with the same orientation as the electron Larmor frequency. The resulting truncated rotating frame Hamiltonian, following [24] is

$$\hat{\mathcal{H}}_S^r = \hbar(\omega_{0S} - \omega_m) \hat{S}_z + \hbar \omega_{1S} \hat{S}_{x'} \quad (1.1)$$

Alternatively, using circularly polarised microwaves in which the magnetic field rotates and has the form $B_1(\cos \omega_m t \mathbf{x} + \sin \omega_m t \mathbf{y})$, and following a similar transformation as above also yields exactly the same rotating frame Hamiltonian. Computing the time averaged Poynting vector for both these cases, we have

$$\begin{aligned}
 \mathbf{S}_{\text{avg}}^L &= \frac{\int_0^{2\pi/\omega_m} |\mathbf{E}| |\mathbf{B}| dt}{\mu_0^2 \int_0^{2\pi/\omega_m} dt} \mathbf{z} \\
 &= 4 \frac{\eta_0 \int_0^{2\pi/\omega_m} |B_1|^2 \cos^2 \omega_m t dt}{\mu_0^2 2\pi/\omega_m} \mathbf{z} \\
 &= 2 \frac{\eta_0}{\mu_0^2} |B_1|^2 \mathbf{z} \\
 \mathbf{S}_{\text{avg}}^C &= \frac{\int_0^{2\pi/\omega_m} |\mathbf{E}| |\mathbf{B}| dt}{\mu_0^2 \int_0^{2\pi/\omega_m} dt} \bar{\mathbf{z}} \\
 &= \frac{\eta_0 \int_0^{2\pi/\omega_m} |B_1|^2 dt}{\mu_0^2 2\pi/\omega_m} \mathbf{z} \\
 &= \frac{\eta_0}{\mu_0^2} |B_1|^2 \mathbf{z}
 \end{aligned}$$

where η_0 is the free space impedance and μ_0 is the magnetic permeability of free space. Thus, only half the power is required when using circular polarisation as compared to linear polarisation to obtain the same effect on the electron spins. The transition probability W_S for the direct electronic transition due to the Hamiltonian in equation (1.1) is ([24])

$$W_S = \frac{1}{2} \pi \omega_{1S}^2 h(\omega_{0S} - \omega_m)$$

where $h(\omega)$ is the homogeneous EPR lineshape.

For a paramagnetic species with a purely homogeneous EPR spectrum and no spectral spin diffusion, such as BDPA or motionally narrowed TEMPO radicals in liquids, the rate of change of electron polarisation is thus governed only by W_S and the spin-lattice relaxation time T_1 . In the steady state, these two transition rates balance each other, giving the following relations ([25])

$$\langle \hat{S}_z \rangle = \frac{\langle \hat{S}_z^0 \rangle}{1 + 2W_S T_1} \quad (1.2)$$

$$s = \frac{2W_S T_1}{1 + 2W_S T_1} \quad (1.3)$$

1.2 Solid effect

The solid effect, first reported by Jeffries in 1957 [26], is observed in solids where the nuclei and electrons are coupled through the hyperfine interaction, with the same energy level diagram seen in figure 1.1. As opposed to the Overhauser effect however, in this mechanism, the polarisation transfer is a single step process, in which the zero or double quantum transition is directly excited by microwaves. In order for this to be possible, the hyperfine terms need to be large enough that the electron and nuclear states are ‘mixed’ and are not pure eigenstates of the Zeeman Hamiltonian [25].

As before, the static spin Hamiltonian does not contain terms that can provide the energy needed for these two off-resonance transitions. This energy is derived from off-resonant excitation by microwaves, with angular frequencies of $\omega_m = \omega_{0S} + \omega_{0I}$ and $\omega_m = \omega_{0S} - \omega_{0I}$ for the ZQ and DQ transition respectively. Thus, the full spin Hamiltonian

$$\hat{\mathcal{H}} = \hbar\omega_{0S}\hat{S}_z - \hbar\omega_{0I}\hat{I}_z + 2\hbar\omega_{1S}\cos\omega_m t\hat{S}_x + \hbar\hat{\mathbf{S}} \cdot \hat{\mathcal{A}} \cdot \hat{\mathbf{I}}$$

needs to be used to study this transition. Importantly, as the microwaves are off resonance, there is a large residual electron Zeeman term even in the rotating frame, and the net magnetic field in this frame is tilted with respect to the x-axis. In the rotating frame, the angular frequency vector along the x-axis for high power microwave irradiation is typically on the order of several MHz, while that along the z-axis is approximately ω_{0I} , which is several hundreds of MHz. With the assumption that $\omega_{1S} \ll \omega_{0I}$ and following [24] for the derivation of the transition probabilities, we have

$$W_0^{\text{SE}} = \frac{1}{8}\pi|A_{z+}|^2 \frac{\omega_{1S}^2}{\omega_{0I}^2} h(\omega_{0S} + \omega_{0I} - \omega_m) \quad (1.4)$$

$$W_2^{\text{SE}} = \frac{1}{8}\pi|A_{z+}|^2 \frac{\omega_{1S}^2}{\omega_{0I}^2} h(\omega_{0S} - \omega_{0I} - \omega_m) \quad (1.5)$$

for the ZQ and DQ transition respectively, where A_{z+} is the off-diagonal element of the hyperfine tensor that is associated with nuclear spin flips and $h(\omega)$ is the homogeneous EPR lineshape, as before. The signs of the enhancement can be deduced from figure 1.1. Assuming 100 % electron polarisation, energy levels 1 and 4 are populated, while 2 and 3 are empty. The DQ transition at $\omega_m = \omega_{0S} - \omega_{0I}$ populates the nuclear ground state 2 at the expense of the excited state 4, causing increased nuclear polarisation and positive enhancement. The ZQ transition at $\omega_m = \omega_{0S} + \omega_{0I}$ populates the nuclear excited state 3 while depopulating the ground state 1, inverting the nuclear polarisation and producing negative enhancement. This is summarised in figure 1.3 below.

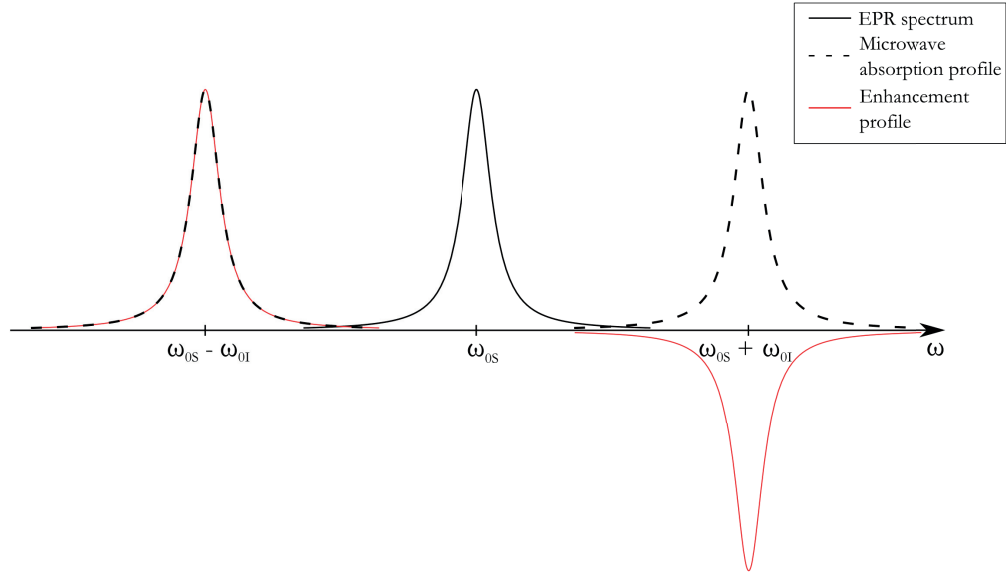


Figure 1.3 – A Lorentzian EPR line, along with predicted microwave absorption and enhancement profiles for the solid effect

As the solid effect does not involve saturation of the single quantum transitions, the microwave power needed does not depend upon the electron T_1 . However, from equation (1.4), we see that the transition probability scales inversely as the square of the external magnetic field. Thus, the microwave power needed to saturate the solid effect transitions scales with field and becomes prohibitively large as we go to high fields. The process described here holds true for EPR lines with widths smaller than the nuclear Larmor frequency. If the linewidth is similar to or wider than the nuclear Larmor frequency, the so called unresolved solid effect is observed, where the two lobes seen in figure 1.3 overlap, and partially offset each other in the region of overlap. However, the peak positions of the two lobes are always separated by $2\omega_{0I}$.

1.3 Cross effect

In solids where electron spins experience strong dipolar coupling with one another, a different DNP mechanism called the cross effect is observed. One example of such a system is a large concentration of paramagnetic impurities with a high g-factor anisotropy dispersed in a solid matrix. In this case, the EPR spectrum is not the homogeneous lineshape function $h(\omega)$, but is given by a powder pattern $g(\omega)$ which is an envelope of contributions from all the possible orientations of the paramagnetic centre. Individual ‘spin packets’ within this powder pattern are coupled to each other through electron-electron dipolar coupling. If the total width of this inhomogeneous line is larger than the nuclear Larmor frequency, two such spin packets can be found with a spectral separation equal to ω_{0I} , as in figure 1.4.

A pair of spins in these two spin packets, if coupled to a nearby nuclear spin, can then undergo

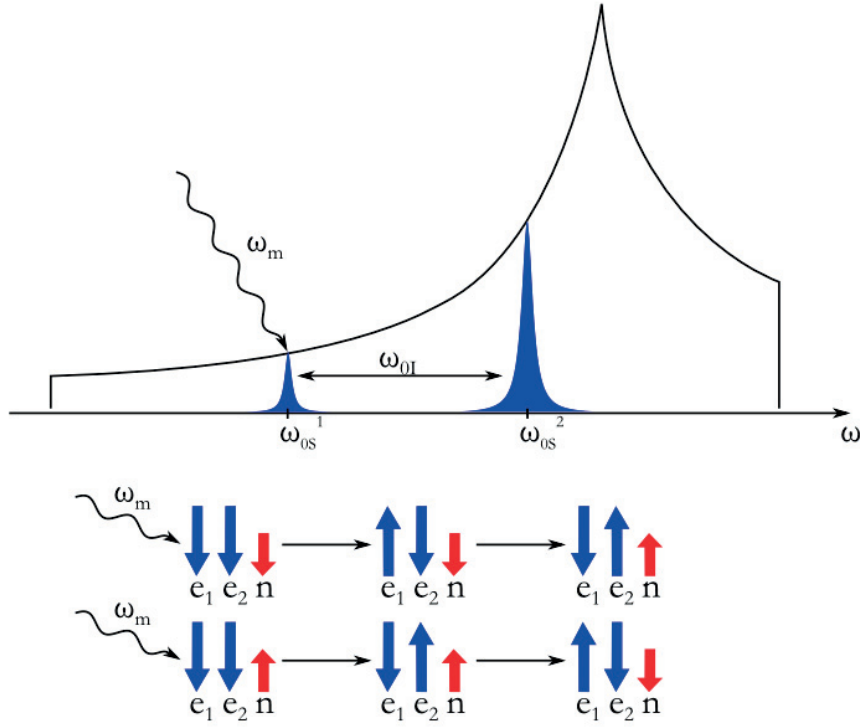


Figure 1.4 – A schematic powder pattern EPR line, with two electron spins separated by ω_{0I}

a triple spin flip process as shown in the schematic. This results in two matching conditions for the microwave frequency: $\omega_m = \omega_{0S}^1$ which results in a positive enhancement, or $\omega_m = \omega_{0S}^2$ which results in a negative enhancement. Thus, the frequency profile of the enhancement is entirely confined within the inhomogeneously broadened EPR line $g(\omega)$. Moreover, for this simple spin system of two electrons and one nucleus, there will be an angular frequency ω_{0S}^0 within the EPR line, where there is equal probability of finding coupled electrons at $\omega_{0S}^0 - \omega_{0I}$ and at $\omega_{0S}^0 + \omega_{0I}$, and the net enhancement due to these two effects will be zero. Notice that finally, for $\omega_m < \omega_{0S}^0$ we will observe positive enhancement and for $\omega_m > \omega_{0S}^0$ we will have negative enhancement.

A complete treatment of the cross effect must necessarily involve spectral spin diffusion of both electrons and nuclei. Thurber and Tycko [27] have treated the simpler three spin system above and obtain the following expression for the transition probability of the triple spin flip

$$W^{\text{CE}} \propto \frac{D^2(|A_{zx}|^2 + |A_{zy}|^2)}{\omega_{0I}^2}$$

where D is the dipolar coupling constant between electrons and A_{zx} and A_{zy} are elements of

the hyperfine tensor. Unlike in the solid effect, this transition probability does not depend on the microwave irradiation, and the cross effect transition occurs even in the absence of microwaves. As a result, the role of microwaves is limited to saturation of the electronic single quantum transitions, and in general DNP through the cross effect requires much smaller microwave powers than the solid effect at high fields. Hu et al present a detailed diagonalisation of the three spin Hamiltonian, together with the interaction with the microwave field [28], and argue that the simple triple spin flip above represents only one of the many polarisation transfer pathways that occur in such a system. They propose that contributions from the different dipolar interactions involved thus compensates for the magnetic field dependence seen in the expression above. However, the one remaining manner in which the magnetic field influences efficiency of the cross effect is through the microwave matching conditions. As the width of an EPR spectrum that is dominated by g-factor anisotropy increases linearly with B_0 , the amplitude of $g(\omega)$ correspondingly scales as B_0^{-1} . This reflects in the probability of finding electrons corresponding to the triple spin flip matching conditions, and thus the efficiency of the cross effect can be expected to decrease with increasing magnetic field as well.

2 DNP and EPR Instrumentation

2.1 DNP-NMR Spectrometer

The NMR experiments were performed on a home built NMR spectrometer with a SpinCore RadioProcessor card for pulse generation and triggering, a GaGe 14-bit digitiser and a home built arrangement of signal receiver and pre-amplifier. The NMR magnet is an Oxford Instruments superconducting 14 T magnet set at 9.3 T fitted with a Variable Temperature Insert for low temperature operation. The NMR probes were home built, singly tuned tank circuits with different coil geometries depending on the samples and nuclei studied. The tank circuits were fitted coaxially at the end of a 1.5 m long corrugated waveguide assembly designed by SwissTo12 SA, to bring the microwave irradiation into the NMR cryostat and down to the sample position for the DNP experiments. A second 3.5 m long waveguide section brings the microwaves from the gyrotron to the top of the NMR magnet, where a 90° miter bend couples the two lengths of waveguide. The corrugated waveguides used are expected to have propagation losses of about 0.5 % m⁻¹ [29]. Losses after 0.8 m of waveguide were measured by de Rijk et al. [30] to be less than 2 %. We thus expect a total power loss from source to sample of less than 10 % in all our DNP experiments, allowing for possible misalignment and coupling losses at insertion and exit.

2.1.1 Gyrotron source for high power 260 GHz radiation

DNP experiments using a variety of hyperpolarisation mechanisms have been reported in the past, to enhance the sensitivity of NMR measurements at low fields [31]. Saturation of the relevant transitions was possible due to the ready availability of oscillators, amplifiers and high Q-factor resonators at low frequencies. The recent introduction of gyrotron sources to satisfy the power requirements of DNP at sub-terahertz frequencies has made it possible to extend the technique to high field NMR [10]. In order to meet the wide range of power requirements of our DNP experiments, a gyrotron source operating at 260 GHz was designed and installed at the LMPN by the Swiss Plasma Centre at EPFL.

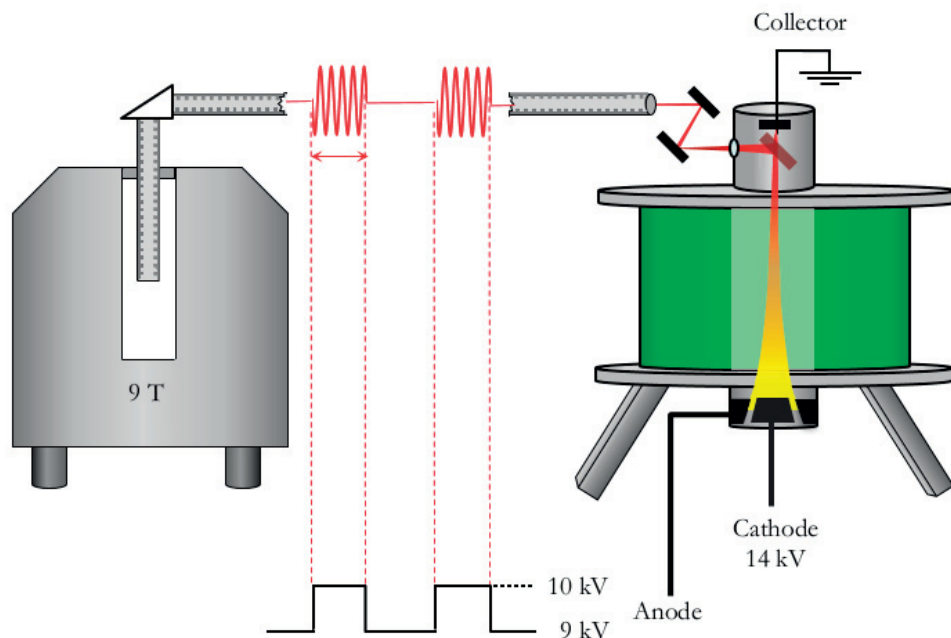


Figure 2.1 – The gyrotron DNP-NMR setup, with the gyrotron magnet shown in green, the NMR magnet in grey and the corrugated waveguide assembly

The gyrotron cavity is housed in the central bore of a Cryogenics cryogen free superconducting magnet operating nominally around 9.4 T. A triode Magnetron Injection Gun emits and accelerates electrons into the cavity where a longitudinal $TE_{7,2}$ mode is excited, and the emitted radiation leaves the cavity through a Vlasov launcher, a mirror assembly and a sapphire window. After exiting the cavity, the electron beam is recovered at an isolated, water cooled collector [32]. The frequency and power of the emitted microwaves can thus be tuned through a combination of three parameters - the magnetic field, the anode voltage, and the filament current used to heat the cathode. While the magnetic field provides the broadest range of stable operating points, with frequency tunability of more than 1 GHz as seen in figure 2.2, the other two parameters can be varied much more rapidly and can be externally triggered. During normal operation as shown in figure 2.3, the magnetic field and filament current are brought to the values corresponding to the desired operating point. The anode voltage is then ramped down to a so-called 'blocking' position. At this voltage, which is usually within 1 kV of the calculated target anode voltage, there is a steady electron beam without any microwave output. From this position, the anode voltage can be rapidly switched under an external trigger to the target voltage and back, resulting in pulses of microwave output that are synchronised

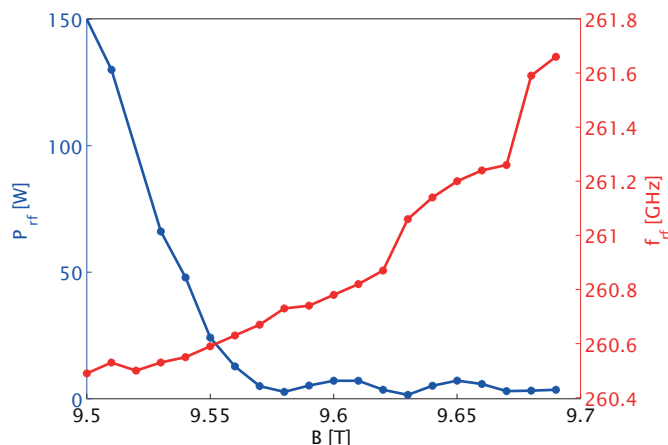


Figure 2.2 – Output frequency and power of the gyrotron as a function of magnetic field

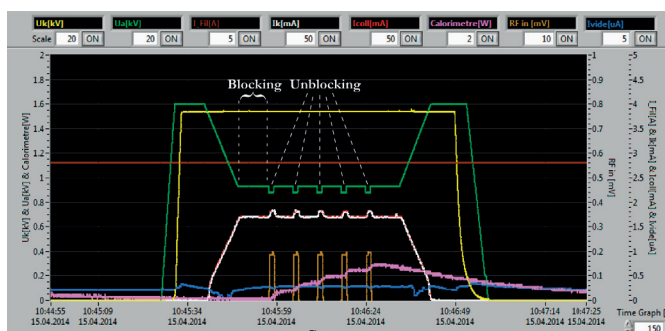


Figure 2.3 – Rapid switching of the anode voltage, in green, resulting in pulsed operation of the gyrotron. Also seen are the cathode voltage in yellow, the cathode current in white, the filament current in brown, the output as measured by the heterodyne receiver in amber, the power measured by the calorimeter in pink and the vacuum level from the ion pump in blue

with the NMR spectrometer. In the ‘blocking’ position, the filament current is controlled in a feedback loop with the measured cathode current to maintain stable operation. The long term stability of the frequency is within 6 MHz of the set point. The beam output can be deflected using a mirror to a diagnostic system consisting of a calorimeter for a simple measurement of the power, and a heterodyne receiver for more precise measurements, including of the frequency.

For certain DNP experiments, such as the frequency modulated Cross Effect and the Integrated Solid Effect [33] [34], it is desirable to rapidly sweep the microwave frequency through a range of values in place of monochromatic irradiation. To achieve this, during the ‘unblocking’ phase of operation, an additional software generated triangular waveform is added to the anode voltage and the microwave frequency thus follows the anode voltage. A characterisation of the resulting frequency profile of the gyrotron, as well as its effect on the Cross Effect DNP enhancement is shown in section 3.1.4. The waveform provided to the high voltage power

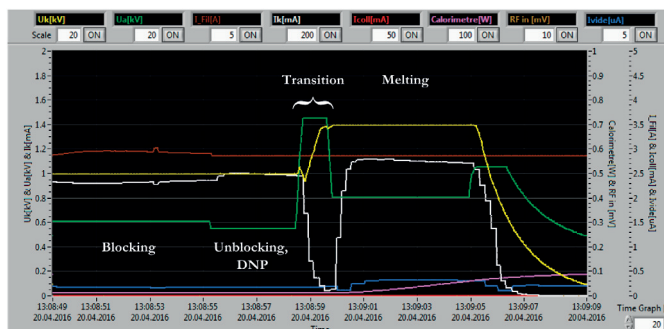


Figure 2.4 – A test of the temperature jump DNP experiment. The gyrotron was switched off after the melting phase for the test, but the cycles can be repeated for signal averaging. The colours are as in figure 2.3

supply can also be generated externally by dedicated hardware, and arbitrary shapes can be used to achieve chirped output. The maximum modulation depth is restricted by the gyrotron's parameter space of stable anode voltages about the chosen operating point. The maximum modulation rate, on the other hand, is hardware limited by the response time of the high voltage power supply used and we were able to achieve a maximum modulation rate of about 14 kHz with our hardware.

The flexibility provided by the ability to control the gyrotron output through the anode voltage lends itself to other exotic experiments such as Temperature-Jump DNP [35], where the frozen sample is melted immediately after hyperpolarisation, to obtain large sensitivity enhancement in liquid state spectra. In place of the infra-red laser used by Joo et al. to melt the sample however, the rapid tunability of the anode voltage enables us to use the gyrotron itself for both hyperpolarisation and for melting [36]. This is achieved in the following manner, as illustrated in figure 2.4. The gyrotron is first tuned to low power operation at the frequency desired for hyperpolarisation. After the trigger from the NMR spectrometer signalling the end of the DNP build-up time is received, the anode voltage is immediately changed to a value corresponding to much higher output power in order to melt the sample. As the frequency of irradiation during this 'melting' phase can be arbitrarily chosen, the gyrotron is tuned for maximum output power, typically 100 W. The sample is exposed to this high power irradiation for a short while, about 1 s, and the anode voltage returns to its 'blocking' value, the NMR signal is acquired, and the sample cools and re-freezes within seconds. This allows for multiple scans of the NMR signal to be acquired by repeating this process with adequate cooling time. This technique can be combined with frequency modulation to achieve higher total enhancement.

2.1.2 Matching Optics Unit and polarisation control

The output of the gyrotron is initially linearly polarised. As circularly polarised light of the appropriate handedness is twice as effective at saturating electronic spins (section 1.1.2), it is desirable to be able to produce circularly polarised light. To achieve this, a universal Matching

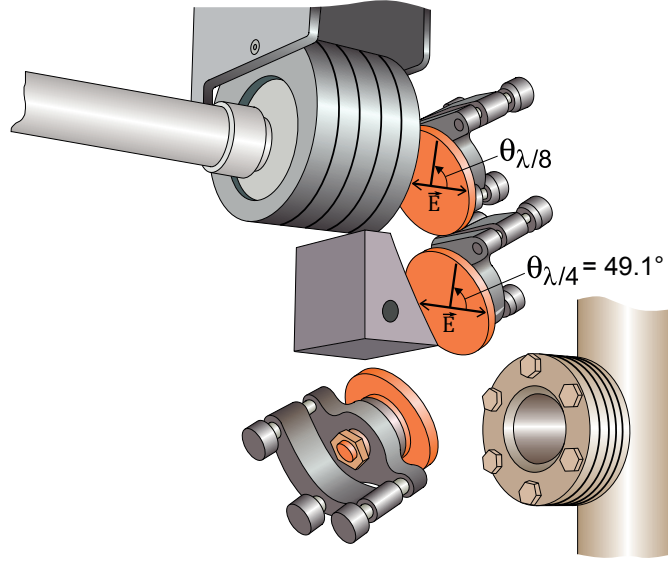
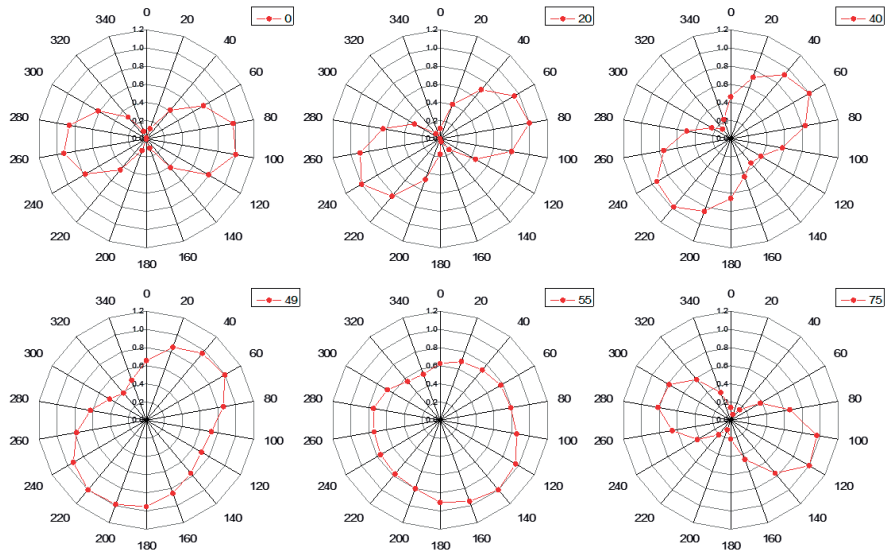


Figure 2.5 – The structure of the MOU. The two mirrors labelled $\lambda/4$ and $\lambda/8$ carry horizontal grooves and can be rotated about their centres. The gyrotron window, silicon attenuators and corrugated waveguide are also shown

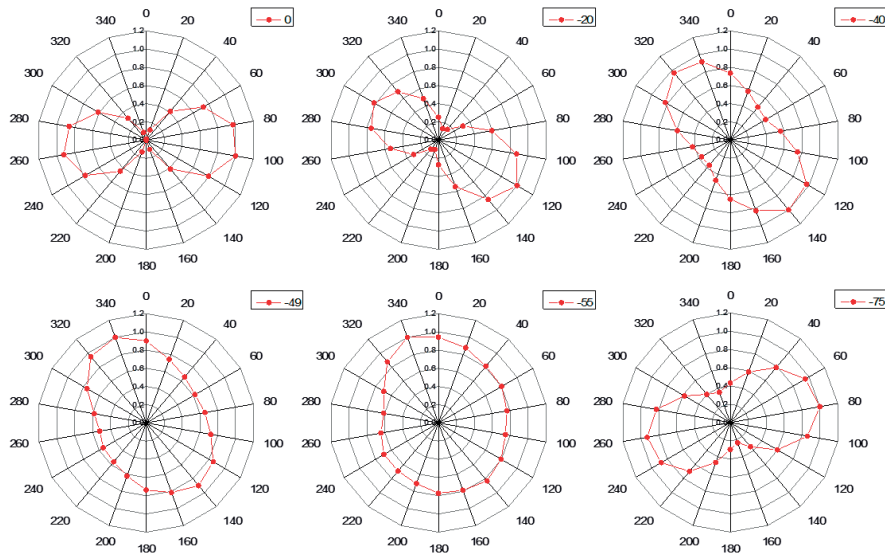
Optics Unit (MOU) consisting of grooved mirrors was designed by de Rijk et al. to couple the gyrotron output into the corrugated waveguides while allowing complete control of the polarisation [37] [29].

The polarisation of the gyrotron output is such that the electric field is initially along the horizontal axis. As illustrated in figure 2.5, after reflection on the mirrors, the electric field vector lies in the plane of both grooved mirrors. The grooves are designed in such a manner that the polarisation of the reflected beam depends on the in-plane angle $\theta_{\{\lambda/4, \lambda/8\}}$ between the grooves and the electric field vector. The grooves in the lower, so called $\lambda/4$, mirror have a depth of 0.31 mm, a period of 0.5 mm and a width of 0.25 mm, and the mirror rotates the incident linear polarisation by an angle depending on $\theta_{\lambda/4}$. At an angle of 49.1° the orientation of the incident polarisation is left unchanged. The grooves in the upper, so called $\lambda/8$, mirror have a depth of 0.214 mm and the same width and period as the other mirror. This mirror changes the ellipticity of the incident polarisation and at an angle of 49.1° , the reflected beam is right circularly polarised.

Although the MOU transforms the incident beam to circular polarisation, the microwaves undergo a 45° reflection at the miter bend used to couple the two lengths of waveguide. As reflection from a metallic surface rotates the polarisation of any light that is not polarised in the plane of the surface, the circularly polarised beam obtained will reach the sample with an elliptical polarisation. In order to correct for this, the effect of the MOU angles on the polarisation of the beam was observed at the sample position, after reflection from the miter bend. A zero bias Schottky diode detector from Virginia Diodes Inc. was mounted in a rotating mount at the end of the vertical section of waveguide, after the NMR coil. As the Schottky



(a) Varying $\theta_{\lambda/8}$ from 0 to positive angles, the polarisation goes towards right circular polarisation



(b) Varying $\theta_{\lambda/8}$ from 0 to negative angles, the polarisation goes towards left circular polarisation

Figure 2.6 – Polar plots of the detected microwave power by a linearly polarised diode detector as a function of detector angle. Plots for varying angles of the $\lambda/8$ grooved mirror are shown

diode is a polarising detector, polar plots of the microwave beam as a function of detection angle were obtained by rotating the detector about the optical axis. Such plots were obtained for elliptically polarised beams with varying ellipticity, produced by rotating the $\lambda/8$ mirror of the MOU from 0 to $\pm 75^\circ$. As seen in figure 2.6, the new angles corresponding to circular polarisation after reflection from the miter bend were found to be approximately $\pm 55^\circ$.

2.1.3 Planar Probe

In addition to interacting with the spin angular moment of electrons through its oscillating magnetic field component, microwave irradiation also causes dielectric heating in the samples used for DNP due to the interaction of its oscillating electric field component with the sample. As microwaves propagate through a dielectric material, it is polarised by the oscillating electric field. This polarisation does not perfectly follow the electric field and experiences dielectric relaxation, which causes dissipation. These two processes are described by a combined complex permittivity

$$\hat{\epsilon} = \epsilon' - i\epsilon''$$

and the dissipation is characterised by the loss tangent

$$\tan \delta = \epsilon'' / \epsilon'.$$

The power transmission is then given by

$$P = P_0 e^{-k\delta z}$$

where k is the magnitude of the wave vector, and is characterised by the power absorption coefficient $\alpha = k\delta$ or its inverse, the penetration depth [38, 39]. This effect is analogous to the skin effect in conductors due to mobile electrons. However, while the skin depth of a conductor decreases as the square root of frequency, the penetration depth due to dielectric loss has an explicit and implicit dependence on frequency through the loss tangent. In the case of water at room temperature, $\tan \delta$ at 260 GHz is approximately 1, and the penetration depth is about 100 μm . For liquid state DNP experiments as in section 3.3, this implies that the large microwave powers of about 100 W are entirely absorbed over a thin 500 μm layer of water. Even for much thinner samples of water, the power deposited in the sample is sufficient to evaporate the water in fractions of a second. This problem is usually solved by the use of resonators, where the electric field and magnetic field components are spatially separated, and the sample can be placed in a region of high magnetic field without experiencing dielectric heating. The small dimensions of microwave resonators at 260 GHz restricts the sample size to nanolitres, however. In our experiments, a novel ‘planar probe’ geometry, designed in collaboration with SwissTo12, was used to overcome the problem of dielectric heating without using a resonator.

As seen in figure 2.7, the probe consists of a copper support within which a square indentation

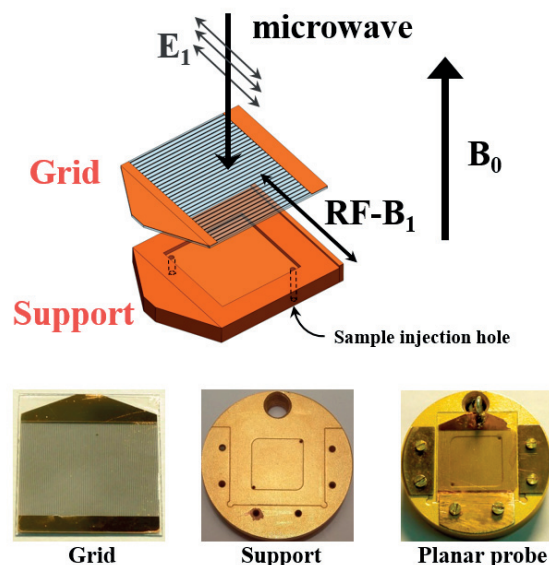


Figure 2.7 – A schematic and photographs of the planar probe

of 1 cm in length and 100 μm in depth is made to hold the sample. The sample is sealed by a 300 μm thick quartz plate, which is etched and carries a deposited grid of 150 copper wires. This grid is transparent to linearly polarised microwaves and also functions as the NMR coil, with the copper block as a ground plane. The copper in the grid is 50 μm in depth and width, and has a period of 100 μm . Lithography and deposition of copper to such high precision was performed at the Center of Micronanotechnology (CMi) at EPFL. The dimensions of the grid, quartz plate and sample holder have been optimised to produce a high microwave magnetic field, while the presence of the ground plane to reflect the microwaves ensures that the electric field is minimised at the sample. The copper block also acts as a heat sink, further reducing heating in the sample. 2D Simulations of the electric and magnetic field distributions in the planar probe geometry described above were performed in COMSOL Multiphysics by Alexandros Dimitriadis of SwissTo12, and the results are shown in figure 2.8. The loss tangent of water was taken to be 0.8 and the real part of the permittivity was assumed to be 6. A beam waist of 9.6 mm in diameter was used for the incident beam, which is determined by the inner diameter of the corrugated waveguide. The peak magnetic field at the sample position for 70 W of power is estimated from the simulation to be about 2.4 G (about 6.7 MHz), as compared to the maximum theoretical value of 2.55 G for a beam undergoing free-space propagation and reflected at a metal surface.

2.2 Martin-Pupplett EPR Spectrometer

A home built quasi optical 260 GHz spectrometer was used to perform EPR measurements at the same field as the DNP NMR experiments [15]. The Martin-Pupplett interferometer design

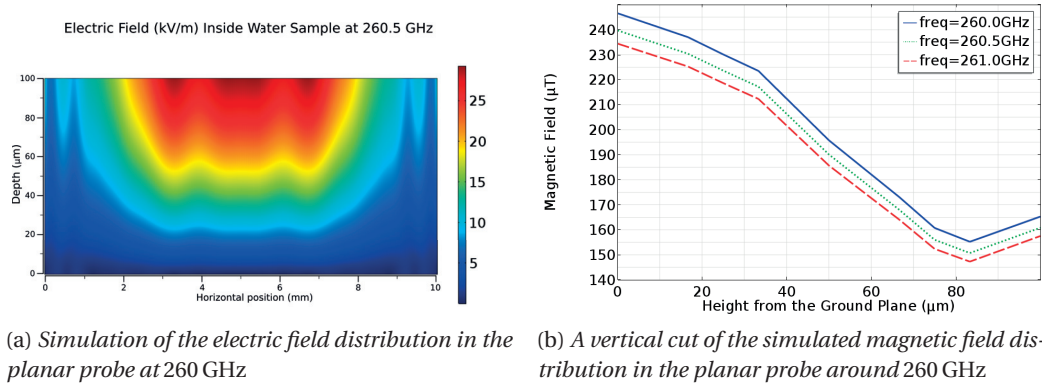


Figure 2.8 – A COMSOL simulation of the electric and magnetic fields for 70 W of input power in the sample space of the planar probe, when filled with water

provides complete control of the microwave polarisation, allowing for possible future use with the DNP setup as well [40]. The interferometer was built on a compact optical board and mounted on top of the NMR magnet at the end of the horizontal waveguide section, as shown in figure 2.9.

The incident beam is reflected by parabolic mirrors around the optical board and arrives at the polarisation splitter, where it is split into two orthogonally polarised segments which enter the two arms of the interferometer. The length of the movable arm is controlled through a Thorlabs motor, and a variable phase is introduced between the two beams by means of the rooftop mirrors. The two segments recombine, and the resultant beam has a polarisation of variable ellipticity as a result of the phase difference introduced between the two arms. The polarisation of the microwaves reaching the arms can thus be continuously varied from right circular (RCP) to elliptical, linear (LP), and left circular (LCP) by changing the motor position. However, as will be seen, LP is preferable to RCP for EPR measurements; LCP does not interact with the sample in any way.

The microwaves that return after reflection at the sample reach the grid labelled linear polariser (in figure 2.10). Here any part of the reflected beam that still carries the same polarisation as the initial incident beam passes through to the Faraday rotator and any part that is polarised perpendicular to the initial beam's polarisation is reflected to the detector. Thus, if there is no change in polarisation at the sample, if the rooftop mirrors produce RCP or LCP, half the incident power will be reflected to the detector, while if the rooftop mirrors maintain LP, no part of the reflected beam will reach the detector. At resonance, the sample absorbs only microwaves of RCP. If the interferometer pathway is set to produce RCP, the reflected beam will also consist of RCP, with a slightly reduced power. The resonance will thus be detected at the detector as a dip in measured signal. If, on the other hand, LP is produced by the interferometer pathway, the microwaves reflected from the sample will be distorted in polarisation, and will be elliptically polarised. This portion of the beam that carries orthogonal polarisation will be reflected to the detector and the resonance will be detected as a rise in

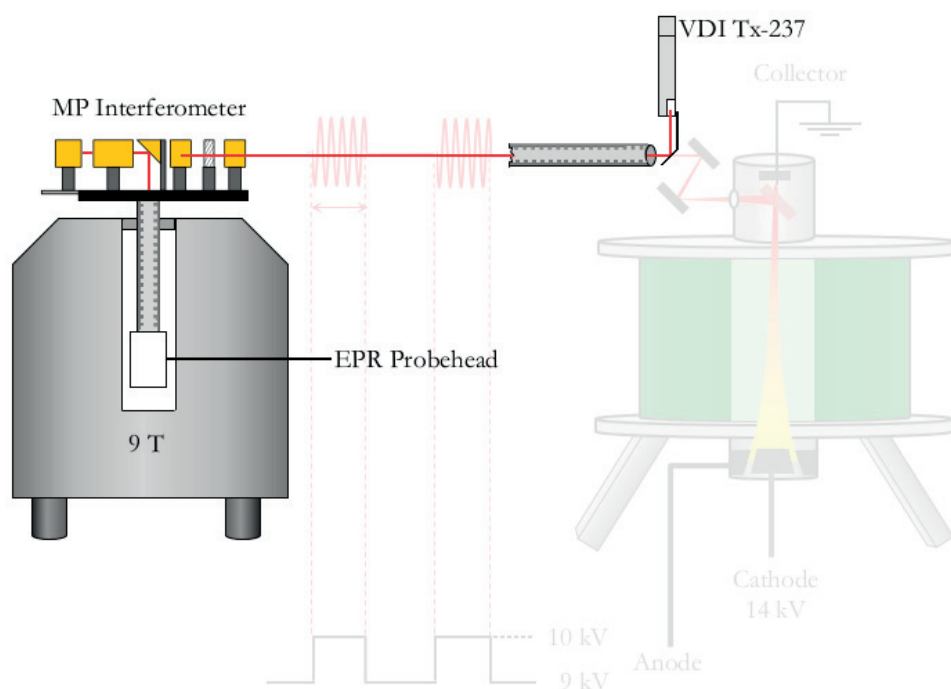


Figure 2.9 – Layout of the Martin-Pupplett EPR spectrometer setup, alongside the existing DNP-NMR setup

signal above a zero background. Thus, an increased sensitivity is expected when LP is used as opposed to RCP. The Faraday rotator and accompanying wire grid act as optical isolators - the polarisation of microwaves passing twice through the Faraday rotator is rotated by 90° and is reflected to the absorber.

The sample holder for the EPR measurements, shown in figure 2.13a, was constructed out of polyether ether ketone (PEEK) to withstand cryogenic temperatures. A planoconvex lens with a focal length of 5 cm focuses the microwaves down to the sample, and an aluminium mirror reflects the beam back. A modulation coil was wound around the PEEK structure at the sample position for field modulated measurements and a programmable AC current source was used to drive the coils at up to 2 kHz. An additional field sweep coil wound on an aluminium frame (figure 2.13b), based on the design of an air core solenoid purchased from ScienceFirst LLC, was used for field-swept experiments and is capable of producing a 100 G field offset. A bipolar current source was used to drive the coil, doubling the available field sweep range. The microwave source used for the EPR measurements was a VDI Tx-237 board from Virginia Diodes Inc., with a frequency range of 245 GHz to 275 GHz and a power output

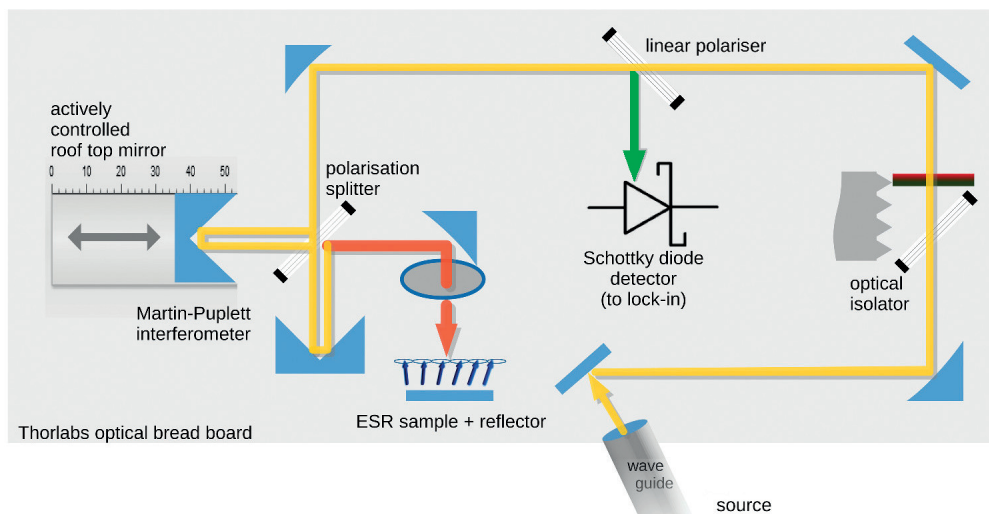


Figure 2.10 – A schematic of the optical path in the Martin-Pupplett interferometer, taken from [15]

of up to 80 mW. A high precision voltage source was used to power the on-board 10 GHz oscillator, allowing for fine frequency control. An auto-heterodyne frequency counter was used to monitor the oscillator in a feedback loop, allowing the final output frequency to be regulated to within 1 MHz. As seen in the figure, the probe head does not contain a resonator to amplify the microwave magnetic field. While this lowers the sensitivity of the spectrometer, this design allows for much larger samples, of up to 5 mm in diameter and 75 μl in volume. Moreover, this allows for frequency agile operation, and a wide range of g-factors from 1.886 to 2.116 are accessible by adjusting the microwave frequency alone.

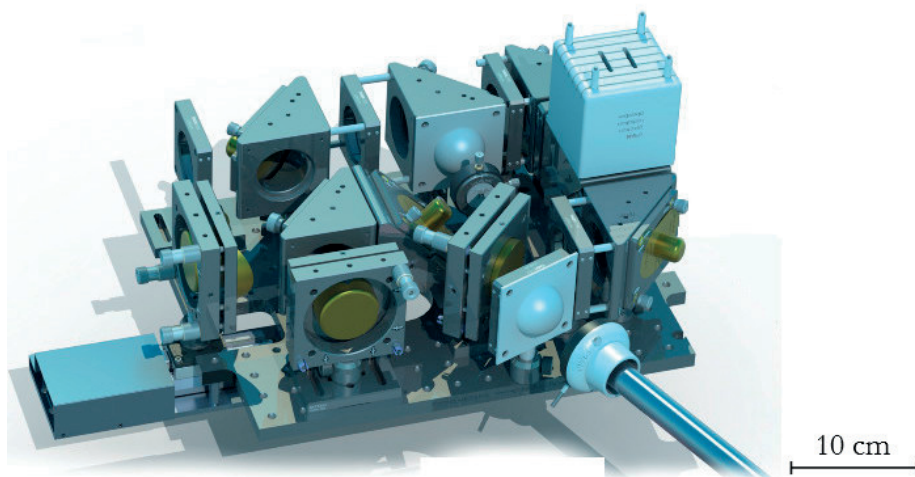


Figure 2.11 – A CAD drawing of the assembled interferometer, taken from [15]

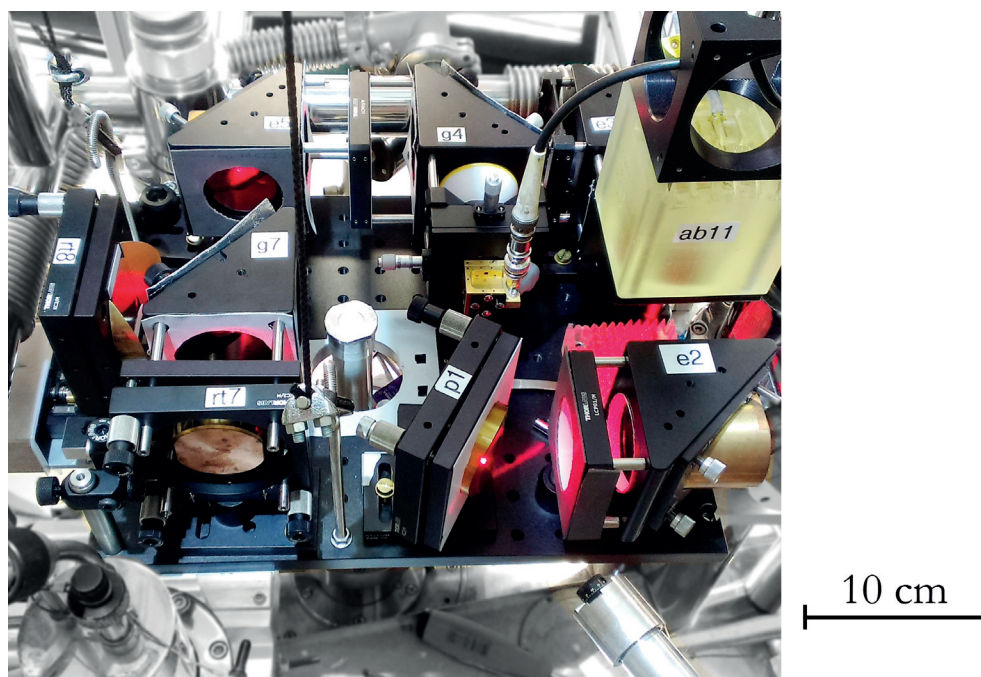
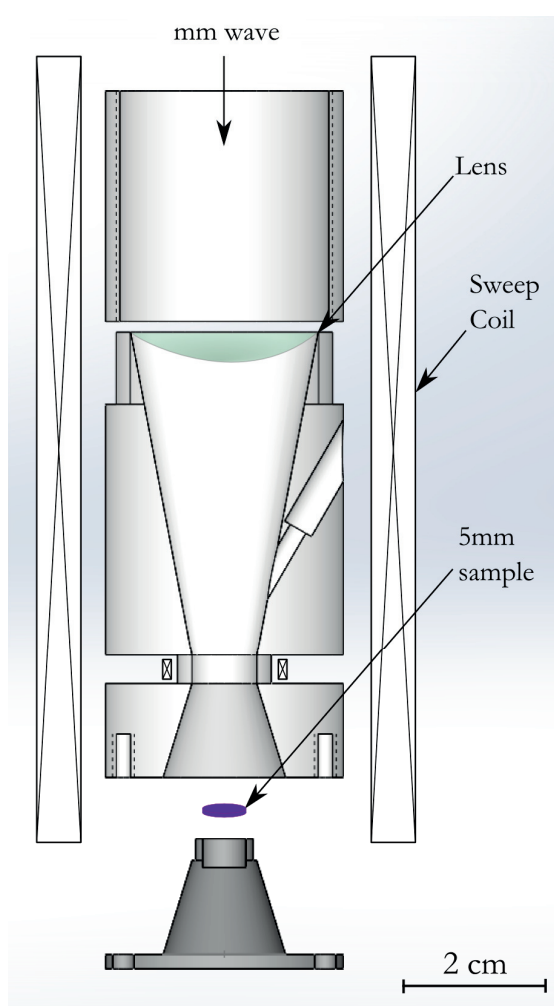


Figure 2.12 – A photograph of the assembled interferometer, mounted above the DNP NMR magnet



(a) The EPR probe head and sample holder



(b) The wire wound resistive sweep coil

Figure 2.13 – The PEEK sample holder and sweep coil used for field-swept measurements

3 DNP Results

3.1 Cross Effect DNP

Preliminary characterisation of the gyrotron DNP setup was done by cross effect ^1H DNP experiments on frozen water solutions. As these experiments were performed at temperatures below 70 K, where the microwave power required is known to be less than 1 W [41], the VDI Tx-237 board was used to complement the gyrotron in some of the experiments. Free standing wire grid attenuators were used to attenuate the gyrotron output for the experiments where polarisation control was not necessary.

3.1.1 Sample preparation

As seen in chapter 1, cross effect DNP requires two dipolar coupled electron spins with resonance frequencies separated by the nuclear Larmor frequency (ω_n). These conditions can be obtained by using specially synthesised biradicals, in which two radicals are grafted onto a tethering molecule to provide a well defined dipolar coupling between them [42]. A less efficient way of producing this is with monoradicals having an inhomogeneously broadened EPR line that is wider than ω_n . At sufficiently large concentrations of monoradicals, the probability of finding two electrons with a large dipolar coupling strength becomes large enough to facilitate the cross effect. This has the drawback of requiring up to 40 mM of radicals in solution, while biradicals are usually employed at concentrations of about 15 mM. It has been shown that biradicals are exceptionally good polarising agents in Solid State Magic Angle Spinning (MAS) DNP experiments [43]. However, under static conditions, not much difference is seen between enhancements in biradical and monoradical solutions [41]. This is attributed to modulation of the biradical spin Hamiltonian during a MAS rotor period, leading to anti-level crossings and a different polarisation transfer mechanism than in static cross effect DNP [44–46]. The (2,2,6,6-tetramethylpiperidin-1-yl)oxyl (TEMPO) nitroxide radical family is well known to chemists, and the radicals are known to have large g-factor anisotropies. Thus, in our experiments, the monoradical 4-hydroxy-TEMPO (TEMPOH) (figure 3.1) was chosen as the polarising agent. This radical is water soluble and has an inhomogeneously

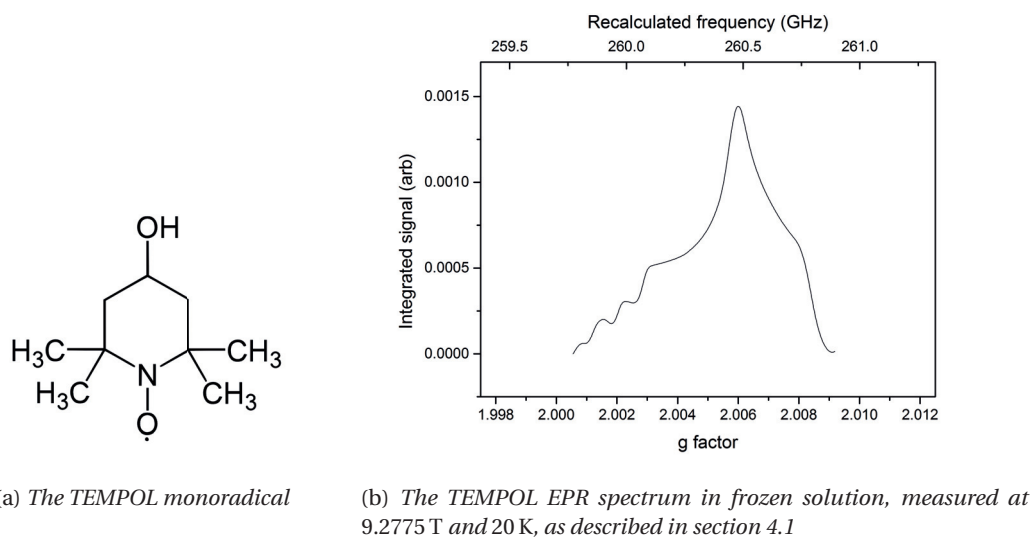


Figure 3.1 – The TEMPOL radical used for cross effect DNP

broadened EPR line about 1.2 GHz in width at 9 T.

The properties of the solvent used to prepare the sample are also critical to obtaining a good DNP enhancement, as it is essential that the radicals be homogeneously dispersed throughout the sample. Most solvents crystallise when frozen. During the crystallisation process, radicals are drawn towards crystal boundaries, and a highly inhomogeneous solid is produced - high concentrations of radicals are found at crystal boundaries and the majority of nuclei do not see paramagnetic spins. The electron spins in these regions of high radical concentration have very short spin lattice relaxation times, making it harder to saturate their EPR resonance and reducing the polarisation transfer. Further, as the majority of nuclear spins are very far from the radicals, their polarisation relies on nuclear spin diffusion over very long distances. Thus, it is necessary to suppress crystal formation while the sample is frozen. This is done by dissolving glass-forming agents such as glycerol, dimethyl sulfoxide (DMSO) and N,N-dimethyl formamide (DMF) in the NMR solvent, which do not crystallise when frozen faster than a critical cooling rate [47]. In our experiments, the sample was prepared with 60 % of glycerol by volume and was frozen by plunging the probe into the cryostat, pre-cooled to 2 K, in order to flash freeze the solution. The samples were loaded into sapphire tubes of 1.3 mm outer diameter and 0.7 mm inner diameter, to achieve maximum thermal contact with the cold helium gas in the cryostat.

To maximise the polarisation transfer from radicals to nuclei, nuclear relaxation pathways other than the triple spin flip mechanism must be minimised. Glassy samples prepared as in the previous section create a homogeneous distribution of radicals, ensuring all the nuclei in the sample have similar magnetic neighbourhoods. For ^1H DNP experiments, as the natural abundance (99.98 %) and gyromagnetic ratio ($42.577 \text{ MHz T}^{-1}$) of protons is large, spin-lattice relaxation mediated by the internuclear dipolar interaction is very efficient. To reduce this,

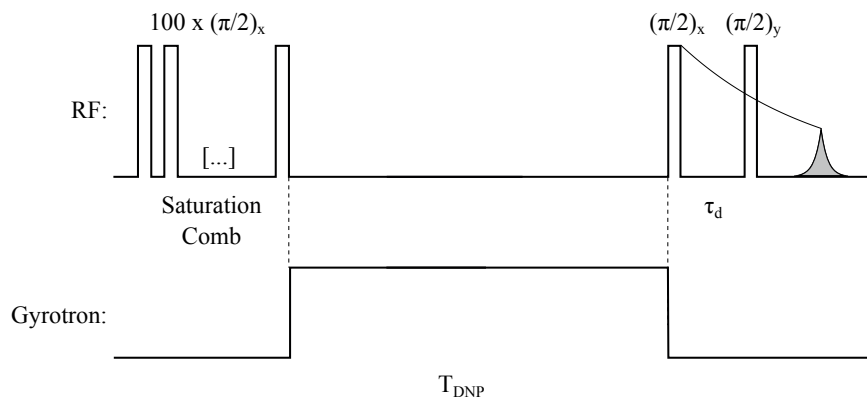


Figure 3.2 – The DNP pulse sequence: T_{DNP} is the irradiation time for polarisation build-up and τ_d is the solid echo delay time

protons in the sample are diluted by using deuterated solvents. An optimum composition of 60 % d8-glycerol, 30 % D_2O and 10 % H_2O by volume, purchased as ‘DNP Juice’ from DyNuPol, was used as solvent. 40 mM of TEMPOL, purchased from Sigma-Aldrich, dissolved in this solvent was used for most of the DNP measurements.

3.1.2 1H DNP

About 2 μ l of the sample, as prepared in the previous section, was frozen to 20 K and the thermal equilibrium 1H NMR was measured using a solid echo sequence with an echo delay of 250 μ s to differentiate the sample signal from the background signals observed. The nuclear spin-lattice relaxation time T_{1n} was measured using a saturation recovery experiment to be 23 s. The DNP enhanced signal was obtained with the following pulse sequence, shown in figure 3.2: a saturation comb, consisting of $100 \left(\frac{\pi}{2}\right)_x$ pulses was applied, followed by a recovery time of $5 \times T_{1n}$. The fast switching capability of the gyrotron enabled us to trigger the microwave output from the NMR spectrometer and the irradiation was restricted to the recovery time. A solid echo sequence, identical to that used to measure the thermal equilibrium signal, was applied at the end of this irradiation time and the resulting signal was acquired. The sample was allowed to cool to ambient temperature over an additional waiting time of 3 to 5 times the irradiation time at the end of each acquisition period. The enhancement, ϵ , was determined using the echo integrals I_{mw} , I_{th} as

$$\epsilon = \frac{I_{mw} - I_{th}}{I_{th}}$$

The enhancement observed varies with the microwave frequency applied, and this enhancement profile, measured using the VDI Tx-237 at 20 K, exhibits the characteristic features

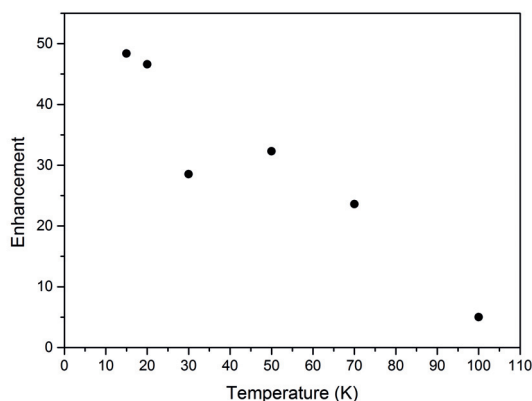


Figure 3.3 – Maximum ^1H enhancement obtained as a function of sample temperature at 260.73 GHz and 9.277 T

of cross effect DNP, as seen in figure 3.5. The maximum positive enhancement is about 20 % larger than the value of the maximum negative enhancement. While the full extent of this DNP spectrum was out of the frequency range of our gyrotron at this field, we were able to reach the frequency corresponding to maximum negative enhancement at 260.725 GHz, where an enhancement of about -40 was obtained. As the depolarisation of the electron spins depends on the microwave power applied, the enhancement increases with increasing microwave power until a ‘hole’ is burned into the EPR spectrum, corresponding to complete depolarisation in the spectral neighbourhood of the microwaves. In practice, dielectric heating increases the sample temperature and reduces the DNP efficiency, causing the enhancement to reach a maximum and then reduce at higher applied powers. As the T_{1e} of the TEMPOL radicals in frozen solution increases with decreasing temperature, the microwave power required to maximise the enhancement decreases with decreasing temperature. At 20 K the optimum microwave power was found to be about 120 mW, and increased to about 2 W at 70 K. Of course, as our sample is only cooled through thermal contact with the cold Helium gas, microwave powers of 1 W are enough to cause significant dielectric heating.

3.1.3 Microwave polarisation control

In the previous section, the linearly polarised gyrotron output was directly used for DNP. As seen in section 1.1.2, it would be beneficial to transform this to circular polarisation.

The gyrotron output was passed through the Matching Optics Unit, described in section 2.1.2, with the linear polarising mirror at $\theta_{\lambda/4} = 49.1^\circ$. The circular polarising mirror was varied from $\theta_{\lambda/8} = 0^\circ$ (linearly polarised) to $\theta_{\lambda/8} \approx 50^\circ$ (right circularly polarised, as per figure 2.6a). As the wire grid attenuator rotates the polarisation of the transmitted beam out of plane of the MOU mirrors, doped Silicon attenuators were used instead and an attenuated power of 15 mW was used for the experiment. The enhancement obtained was normalised with respect

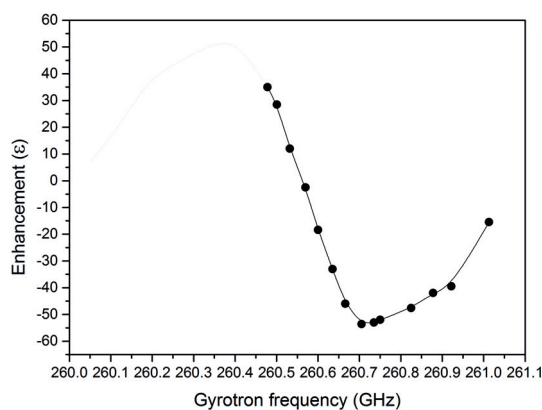


Figure 3.4 – ^1H DNP enhancement as a function of gyrotron frequency, at 20 K and 9.277 T

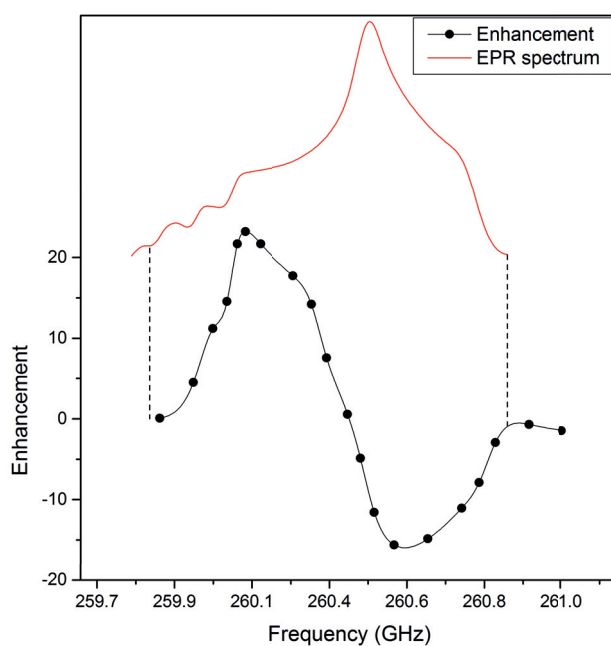


Figure 3.5 – EPR spectrum and DNP enhancement measured with the VDI Tx-237 source, at 9.277 T and 20 K - the lines are a guide to the eye

to that at linear polarisation. The maximum enhancement was obtained at about 40° and was 70 % larger than with linear polarisation. Changing $\theta_{\lambda/8}$ from 0° to -50° , corresponding to left circular polarisation, produced no change in the enhancement (not shown).

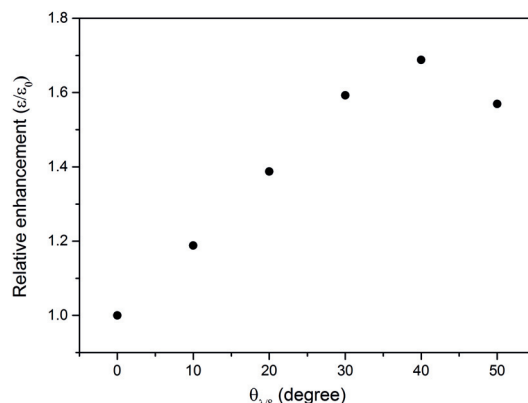
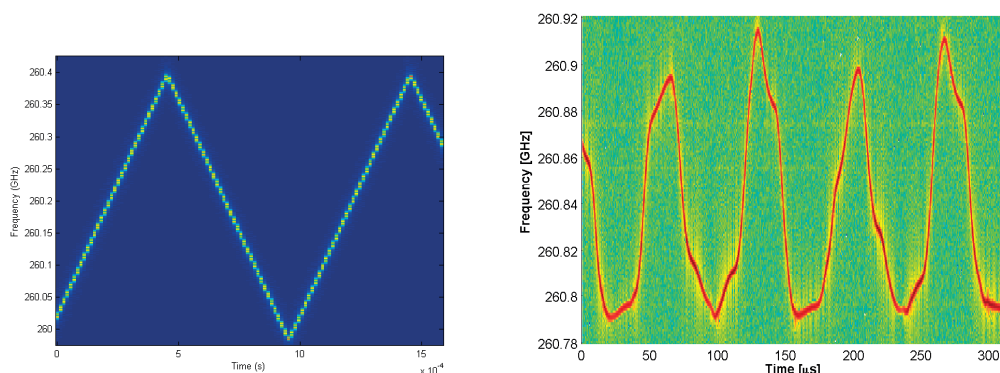


Figure 3.6 – ^1H DNP enhancement as a function of $\lambda/8$ mirror angle, obtained at 20 K and a microwave power of 15 mW

3.1.4 Frequency modulated DNP

As cross effect DNP is dependent on saturation of the EPR spectrum of the radicals and the microwave sources used are monochromatic with a narrow bandwidth, electron spin depolarisation is achieved only in a narrow spectral window around the microwave frequency and is propagated only through electronic spectral spin diffusion. As the EPR spectra of radicals used for cross effect DNP are, by necessity, inhomogeneously broadened to a large degree, the width of the enhancement lobes is often as large as 600 MHz at 9 T. Thus, it would seem that if the incident microwave frequency were swept through a portion of the EPR spectrum, more spin packets could be directly depolarised and more efficient saturation of the EPR spectrum could be obtained than with monochromatic radiation. This frequency sweeping must occur at a rate faster than electron spin-lattice relaxation for this process to be effective.

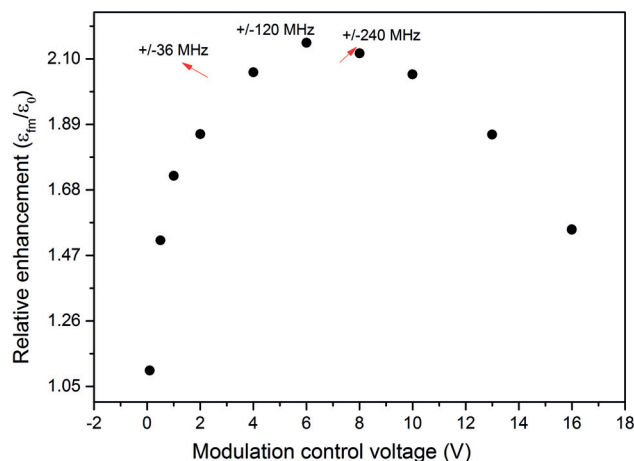


(a) The VDI output frequency for a 6 V, 1 kHz triangular waveform

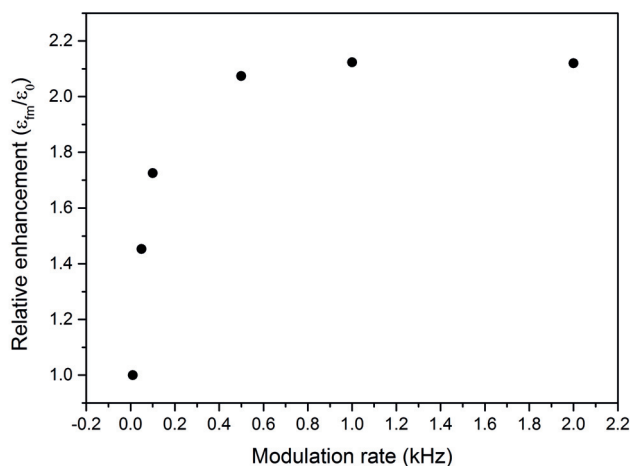
(b) The gyrotron frequency measured using the auto-heterodyne receiver system (from [50])

Figure 3.7 – The frequency profiles of the VDI board and the gyrotron when modulated

This idea was implemented indirectly by sweeping the field using a sweep coil centred around the sample to great effect at 9.4 T by Thurber et al. [41]. More recently, in the dissolution DNP experiments of Bornet et al [48] and in cross effect DNP experiments of Hovav et al at 3.34 T [49], the frequency output of the solid state microwave source was modulated and improvements in the enhancement by a factor of up to 2 and 3 respectively were obtained.



(a) ^1H DNP enhancement as a function of modulation depth



(b) ^1H DNP enhancement as a function of modulation rate

Figure 3.8 – The effect of frequency modulation of the VDI Tx-237 source on the ^1H DNP enhancement, at 20 K and a centre frequency of 260.736 GHz

In our experiments, the frequency output of the VDI Tx-237 source was modulated by applying a triangular waveform at the voltage input port provided for this purpose [50]. The behaviour of the output frequency was analysed by measuring the output of the monitor port of the

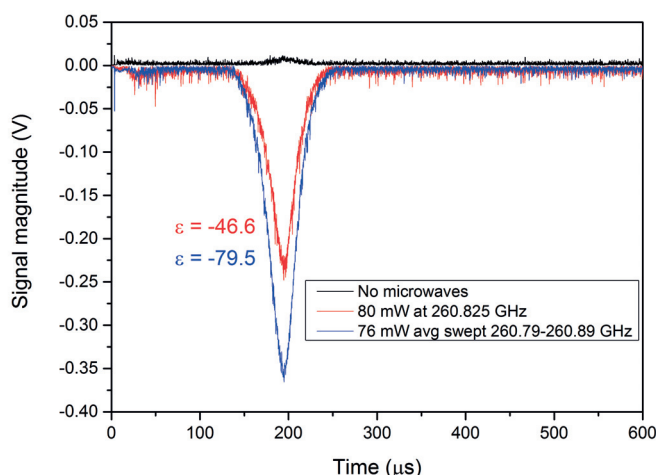


Figure 3.9 – ^1H solid echoes with an echo delay of $150\ \mu\text{s}$ at 20 K and 9.277 T with frequency modulation of the gyrotron

local oscillator on a fast oscilloscope, and multiplying the frequency up by 24, as in figure 3.7a. The maximum depth of the frequency modulation obtainable in this manner is 600 MHz at arbitrary rates. The change in enhancement produced as a function of the modulation rate was investigated at a fixed modulation depth of 120 MHz at 260.736 GHz. Keeping the rate fixed at 1 kHz, the effect of increasing modulation depth on the enhancement was also measured. All the experiments performed with the VDI source were conducted at 20 K due to its low power output of 80 mW.

More interestingly, as seen in section 2.1.1, our gyrotron system is also capable of producing a frequency modulated output. As one of the parameters determining the microwave frequency is the anode voltage, rapidly sweeping the anode voltage repeatedly during the ‘unblocking’ phase effectively modulates the frequency. As the tuning range of the gyrotron based on the anode voltage alone is limited, the maximum depth of frequency modulation is fairly low, about 50 MHz at 260.840 GHz (figure 3.7b). Moreover, the power output is not constant, also varying as a function of the anode voltage. The frequency modulated DNP experiments with the gyrotron used microwaves that were swept from 2 W at 260.790 GHz to 0.45 W at 260.890 GHz and then attenuated down in power using reflective silicon attenuators when necessary.

3.1.5 Analysis of cross effect DNP

The ^1H DNP NMR enhancements obtained by the cross effect satisfactorily match expectations based on the theory. Figure 3.5 shows the characteristic cross effect enhancement dependence on the irradiation frequency, with the enhancement map limited by the width of the EPR spectrum. The enhancement is seen to increase as the temperature decreases in figure 3.3,

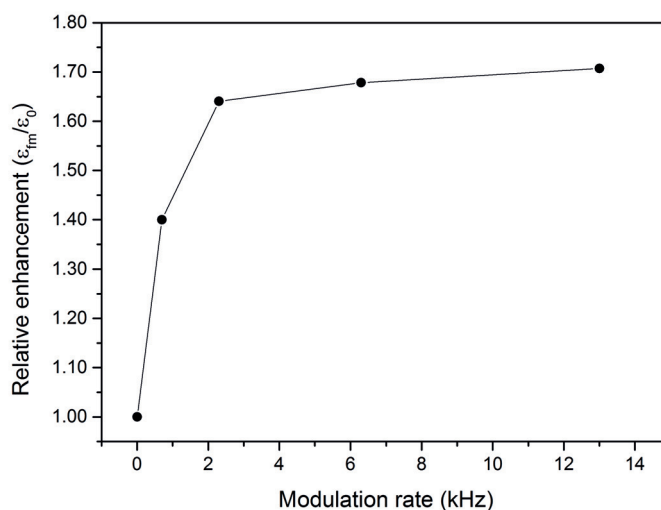
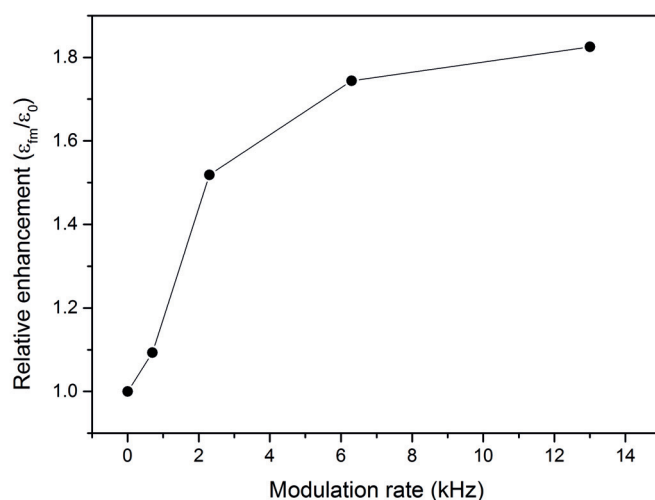
(a) ^1H DNP enhancement as a function of modulation rate at 20 K(b) ^1H DNP enhancement as a function of modulation rate at 70 K

Figure 3.10 – The effect of gyrotron frequency modulation on the ^1H DNP enhancement, at an irradiation frequency of $260.840\text{ GHz} \pm 50\text{ MHz}$. The lines are a guide to the eye. The frequency modulated enhancements were compared to the unmodulated enhancement obtained at a frequency of 260.825 GHz and a power approximately equal to the average power under modulated conditions.

consistent with previous reports for static cross effect DNP in similar temperature ranges [41, 51]. This trend is, in general, due to a variety of factors such as the rates of the triple spin flips involved in the polarisation transfer mechanism. However, one important factor is the increase in T_{1e} as temperature decreases, leading to easier saturation of the EPR spectrum at lower microwave powers, in turn leading to less dielectric heating.

Figure 3.6 shows the increase in enhancement observed when the proportion of circular polarisation in the incident microwaves is increased. However, the maximum occurs at a slightly lower angle than that obtained for circular polarisation in figure 2.6a, and the increase in enhancement is slightly lower than the expected 100 %. This is likely due to distortion in the polarisation at the sample position, possibly due to reflections from the NMR coil. Moreover, sapphire is known to exhibit uniaxial birefringence perpendicular to its c-axis. As a result, any electromagnetic waves polarised along the c-axis see a different dielectric constant as compared to waves polarised perpendicular to it. As the sapphire tube used has its c-axis along the length of the tube, and the microwaves are incident on the curved surface of the tube, the polarisation at the sample will be further distorted and not purely circular. This also explains the fact that the enhancement does not reduce to 0 at the angle corresponding to left circular polarisation.

The frequency modulation experiments with the VDI source and the gyrotron at 20 K show the same qualitative behaviour, with the enhancement initially increasing with increasing modulation rate and then levelling off after a point. This critical rate above which the enhancement levels off is seen to be higher at higher temperatures (figure 3.10b). This is to be expected, as the T_{1e} is expected to increase as temperature decreases, causing the frequency modulation effect to be more pronounced at lower modulation rates. It can also be seen from figures 3.8b and 3.10a that this effect is a function of other interdependent factors as well. At the same sample temperature, frequency modulation with the VDI source levels off at about 1 kHz while with the gyrotron, at a different central irradiation frequency and modulation depth, this occurs at 2 kHz. The experiment at 70 K also differs from the others at low modulation rates and displays an inflection point at about 1.5 kHz. This behaviour was reported at 3 T by Hovav et al. [49]. Electronic spectral spin diffusion can produce a similar effect to frequency modulation on the depolarisation of the EPR spectrum, and the effects observed here will hence depend strongly on the concentration of radicals. This dependence was not studied here, but makes detailed comparison with previous literature more difficult.

The dependence of the enhancement on modulation depth is seen in figure 3.8a. At a central frequency of 260.736 GHz the enhancement increases up to a modulation depth of about 120 MHz and then decreases. This can be explained by analysing the enhancement map in figure 3.5. Centred at 260.73 GHz, frequency modulation up to depths of 180 MHz covers the entirety of the negative enhancement lobe. At larger depths, the modulation begins to mix contributions from the positive and negative enhancement lobes, reducing the overall enhancement.

3.2 Solid Effect DNP

The solid effect is another DNP mechanism commonly observed in solids. As the polarisation transfer mechanism only involves a spin flip-flop between one electron-nuclear pair, the conditions required to observe the solid effect are more general than for the cross effect. However, this flip-flop transition rate is inversely proportional to B_0^2 [24]. Hence, effecting this transition requires extremely large microwave powers at high field and it is difficult to obtain high enhancement values. Becerra et al. obtained ^1H enhancements of about 10 (40 with ^{13}C) in 2 % α, γ -bisdiphenylene- β -phenylallyl (BDPA) doped polystyrene, in the first ever high field gyrotron DNP experiments at 5 T [52]. Later experiments improved on these results and Can et al. reported ^1H enhancements of up to 30 using different sample compositions at 9 T [53].

We performed solid effect DNP experiments on a diamond nanopowder sample. In this experiment, an example of endogenous DNP, defects in 20 nm High Pressure High Temperature (HPHT) treated diamond were used to enhance the NMR signals of the surrounding carbon nuclei. The samples had been irradiated with high energy electrons to increase the density of defects. All samples were provided and treated by Dr. Giovanni Dietler of the Laboratory of Physics of Living Matter (LPMV) at EPFL. As the EPR linewidth of this paramagnetic centres is small, the EPR spectrum was measured using the Martin-Pupplett spectrometer in order to tune the gyrotron to high power output at the frequencies desired. The planar probe described in section 2.1.3 was used in order to reduce dielectric heating and dissipate heat. ^{13}C NMR signals were obtained using a single pulse free induction decay (FID) measurement preceded by a saturation recovery pulse sequence as in figure 3.2. Microwaves were irradiated at the solid effect condition of $\omega_m = \omega_e - \omega_n$ during each build up time to record the DNP signal. The negative enhancement lobe of the DNP spectrum was out of the frequency range of the gyrotron, and the power required was out of range of the VDI source.

3.3 Overhauser Effect DNP

The Overhauser effect in liquids has recently seen considerable progress at high fields. The high microwave powers necessary to saturate the EPR spectra in liquids were made available at high fields with the development of specifically designed gyrotrons, and Overhauser enhancements corresponding to scalar coupling between the radicals and nuclei were observed at 5 T by Loening et al. in non-aqueous, non-polar solutions [54]. As the cross-relaxation of protons and radicals in solution is predominantly dipolar in nature, and the loss tangent of water at high frequencies is exceptionally large (the penetration depth is about 200 μm at 260 GHz), Overhauser DNP in water was thought infeasible. However, large ^1H enhancements with dipolar relaxation of up to 80 were recently obtained in very small volumes of aqueous solutions at 9 T using microwave resonators with active cooling, and nitroxide radicals [55–57].

Ever since it was first predicted in 1953, the Overhauser effect has been demonstrated only in

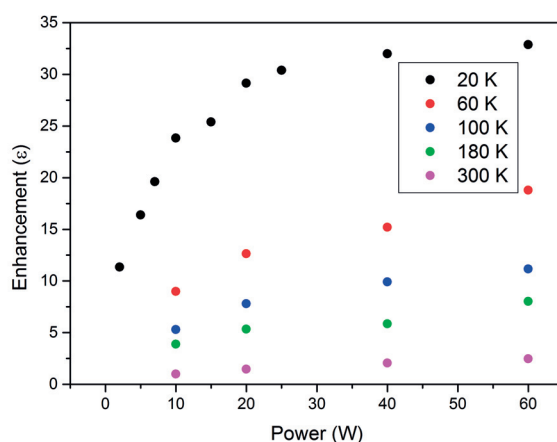


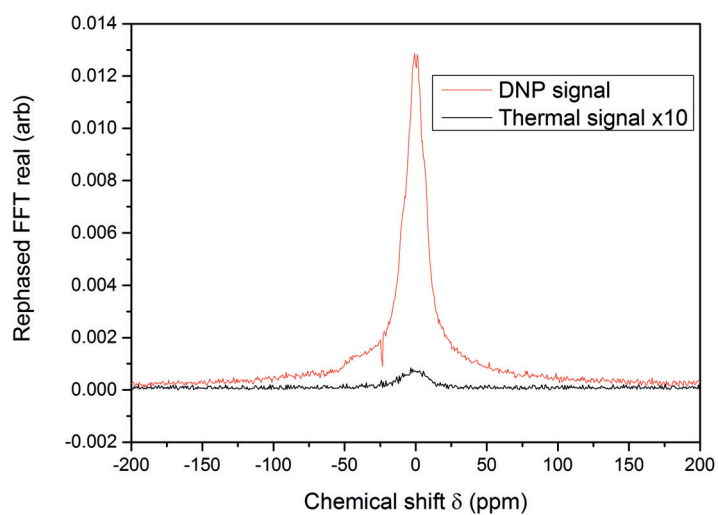
Figure 3.11 – ^{13}C DNP enhancements in the nanodiamond powder as a function of microwave power from 20 K to 300 K - $\omega_n/2\pi = 99.526$ MHz

the case of nuclei immersed in a mobile bath of paramagnetic species. In such systems, such as metals or liquids containing paramagnetic impurities, the rapid motion of the electronic spins ensures short enough correlation times to mediate the mutual electron-nuclear spin flip required for polarisation transfer. While Abragam predicted a similar effect in diamagnetic crystals containing paramagnetic species, with the lattice mediating the spin flips, such enhancement was only experimentally observed on nuclei within the paramagnetic species themselves [23, 58, 59]. Can et al. recently reported the first ever Overhauser enhancements observed in an insulating matrix within which paramagnetic species were embedded, in a BDPA doped polystyrene sample (hereafter referred to as BDPA-PS) [53].

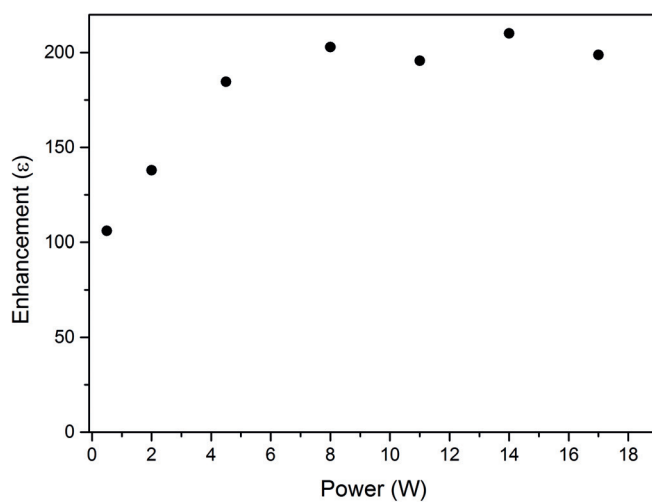
As our gyrotron is capable of high output powers, we were able to perform Overhauser DNP experiments in both liquids and in BDPA-PS, using the planar probe to manage dielectric heating.

3.3.1 ^{31}P DNP in solution

1.6 M of triphenyl phosphine (TPP) dissolved in fluorobenzene was used as the ^{31}P NMR probe. 80 mM of BDPA, purchased from Sigma-Aldrich, was dissolved in the above solution and 10 μL of the sample was injected into the planar probe. The NMR signal was recorded in a single pulse free induction decay (FID) measurement with a repetition time of 5 s. To record the DNP enhanced signal, the sample was irradiated with at 260.51 GHz for 5 s prior to the FID pulse, and the repetition time was increased to 30 s to allow the sample to return to ambient temperature. A positive enhancement was obtained, which increased with increasing microwave power up to a factor of 200 at 8 W and remained stable at higher powers.



(a) ^{31}P NMR and DNP spectra at 300 K with 17 W of microwave power. The thermal spectrum was obtained by averaging over 100 scans and the DNP signal was obtained with 4 scans



(b) ^{31}P DNP enhancement as a function of microwave power at 300 K

Figure 3.12 – Overhauser DNP measurements of the solution of TPP and BDPA in fluorobenzene - $\omega_n/2\pi = 160.184$ MHz, $\omega_m/2\pi = 260.508$ GHz

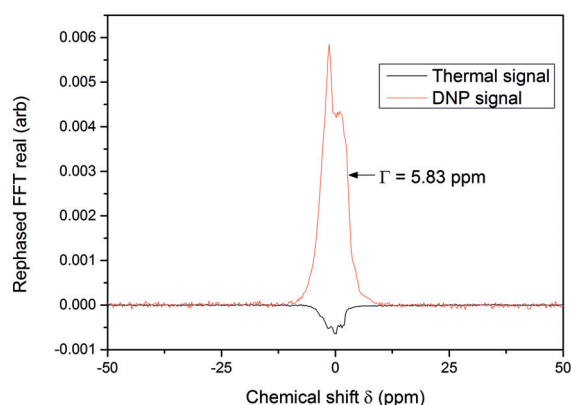


Figure 3.13 – ^1H NMR and DNP spectrum of a solution of TEMPOL in water at 300 K - $\omega_n/2\pi = 395.014$ MHz, $\omega_m/2\pi = 260.437$ GHz

3.3.2 ^1H DNP in solution

80 mM of TEMPOL was dissolved in de-ionised water and 2 μl of this solution was injected into the centre of the planar probe. As before, the NMR and DNP signals were recorded in single pulse FID measurements, with repetition times of 1 s and 5 s respectively. As the highest stable power output of the gyrotron at the desired frequency of 260.437 GHz was 70 W, the microwave beam was not attenuated and was right circularly polarised. As the grid in the original planar probe design acts as a linear polariser for microwave radiation, the design was modified for this experiment. A plain silica glass cover was used in place of the grid, and the RF coil was made by winding copper wire in a solenoidal pattern, with a spacing of about 1 mm around the entire planar probe.

3.3.3 BDPA doped polystyrene

A polystyrene matrix doped with BDPA was prepared by first co-dissolving 2 % by weight of BDPA along with a mixture of 90 % d8-polystyrene (average molecular weight 4700, purchased from Polymer Source Inc.) and 10 % non-deuterated polystyrene (average molecular weight 35000, purchased from Sigma-Aldrich) by weight in toluene. This solution was added dropwise into the sample space of the planar probe and evaporated by directly heating the copper support. In this manner a thin layer of the polystyrene, uniformly dispersed with BDPA, was prepared. The ^1H NMR and DNP signals were obtained using the pulse sequences in figure 3.2. As the rf homogeneity of the planar probe is much poorer than the solenoid coils used for cross effect measurements, complete refocusing of the solid echo was not possible and the echo intensity fell sharply at large delay times, and an echo delay time of 60 μs was used instead of 250 μs . Thus, the true enhancement is possibly larger than reported here as a result of remnant background ^1H signal.

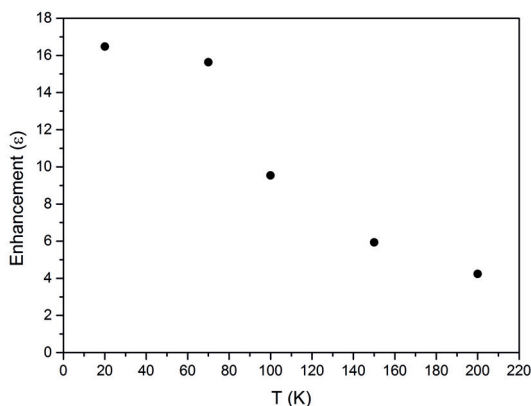


Figure 3.14 – Maximum ^1H DNP enhancements in the BDPA-PS system as a function of temperature, measured at $\omega_n/2\pi = 395.718$ MHz and $\omega_m/2\pi = 260.517$ GHz

The EPR spectrum of the sample, measured in section 4.1.2, was shifted to match the field at which DNP was performed (9.2946 T), and the integrated spectrum is shown alongside the frequency profile of the DNP enhancement in figure 3.15.

3.3.4 Analysis of Overhauser DNP

The positive enhancement of 200 obtained in the ^{31}P experiments with TPP indicates that the Overhauser effect with scalar cross-relaxation is very efficient even at 9 T. However, no noticeable enhancement was seen when triphenylphosphine oxide (TPPO) was used in place of TPP. This confirms studies performed at low fields that reported significant scalar cross-relaxation only in trivalent phosphorus compounds and not in pentavalent phosphorus compounds [60]. It is possible that the lone pair of electrons on trivalent phosphorus that is absent in pentavalent phosphorus is responsible for mediating scalar cross-relaxation, in addition to steric hindrance to approaching radicals. The much lower power needed to obtain enhancements in the ^{31}P experiments as opposed to ^1H reflects the fact that the T_{1e} of BDPA in solution at room temperature is much longer than that of TEMPOL [54, 57].

Using the value of $\omega_{1S} = 2\pi * 6.7$ MHz estimated in section 2.1.3 for a water sample and assuming $T_{1e} \approx T_{2e}$, equation (1.2) derived in chapter 1 for the saturation factor s can be adapted to fit the power dependence of the ^{31}P enhancement as follows, with ϵ_∞ denoting the hypothetical enhancement at infinite microwave power

$$\begin{aligned}\epsilon &= \epsilon_\infty s \\ &= \epsilon_\infty \frac{2\omega_{1S}^2 T_1 T_2}{1 + 2\omega_{1S}^2 T_1 T_2}\end{aligned}$$

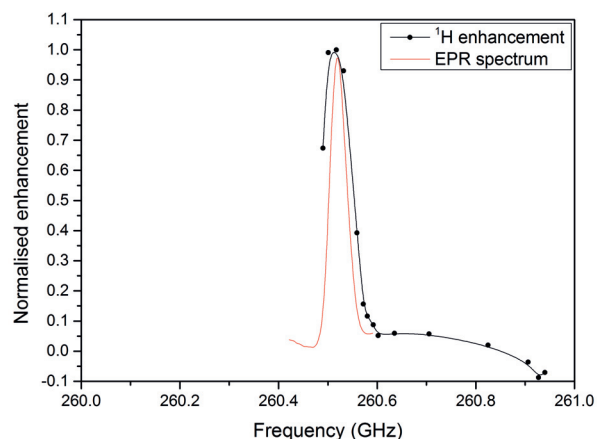


Figure 3.15 – Normalised ^1H DNP enhancements at 20 K in the BDPA-PS system as a function of gyrotron frequency, along with the EPR spectrum of the radical at $\omega_n/2\pi = 395.718$ MHz

Figure 3.16 shows the resulting fit of this hyperbola to the data in figure 3.12b. As the fluorobenzene used in the experiment is a polar solvent like water, the assumptions here are reasonable for an order of magnitude estimate of the T_{1e} of the radical. This yields an asymptotic enhancement value of about 209, and a T_{1e} of about 600 ns.

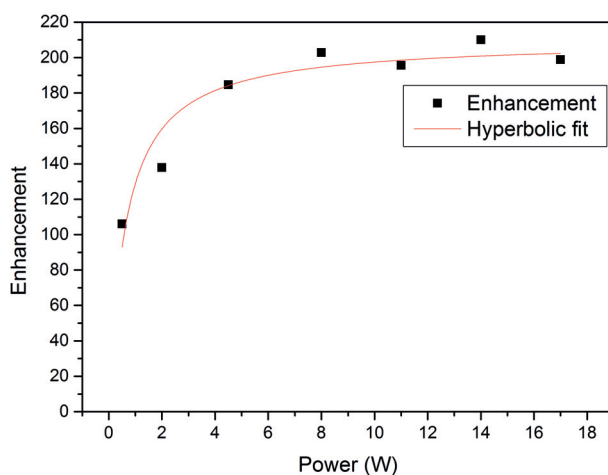


Figure 3.16 – The ^{31}P DNP enhancement as a function of power and the best fit hyperbola, along with fitting parameters

The enhancement of -14 that we obtained in ^1H Overhauser DNP experiments with TEMPOL, while much lower than that obtained by Neugebauer et al. at superheated conditions (160 °C), is identical to their enhancement at 45 °C [57]. From the simulations performed for ambient temperature conditions (figure 2.8a), the microwave magnetic field in the sample space at

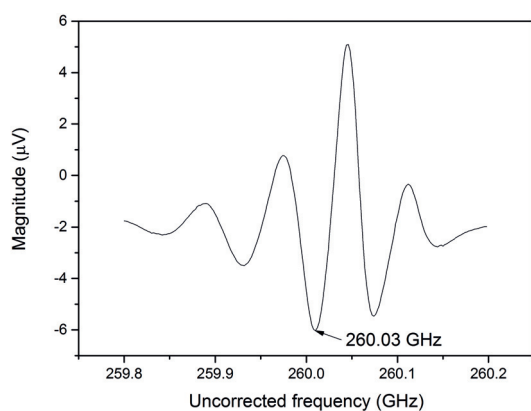
70 W is expected to vary from 2 G to 2.5 G at the centre and decaying to zero at the edges. This field is larger than that used by Neugebauer et al. (1.3 G) to achieve a saturation factor of 0.9, and is moreover right circularly polarised. Thus, we expect the EPR spectrum to be sufficiently saturated at our experimental conditions. We were unable to determine the sample temperature as the linewidth of our NMR spectra due to magnet inhomogeneity is much larger than the temperature dependent ^1H frequency shift, as seen in figure 3.13. As the loss tangent of water increases with increasing temperature, it would become impractical to reliably maintain a high sample temperature through dielectric heating alone, without any active cooling. Thus, although higher enhancements can be expected by raising the sample temperature, this is out of reach of our experimental setup at present. The volume of liquid used in the experiment is the largest reported to date for aqueous samples and demonstrates the effectiveness of the planar probe geometry in reducing dielectric heating.

Figure 3.14 shows an increase in enhancement in the BDPA-PS system from about 4 at 200 K to 17 at 20 K. The frequency dependence of the enhancement, shown in figure 3.15 matches reasonably well with the EPR spectrum, as expected for the Overhauser effect. The EPR spectrum was measured at 300 K while the DNP was performed at 20 K, which explains the difference in linewidths seen. A small negative enhancement due is also noticeable about 400 MHz higher than the EPR frequency, consistent with the solid effect. As the power used was only 4.5 W, the enhancement due to the Overhauser effect is much larger than that due to the solid effect.

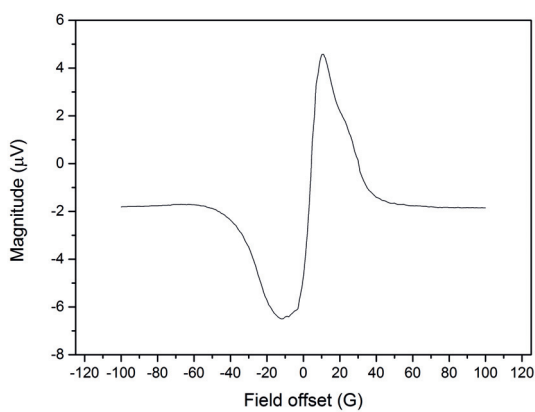
4 EPR Results

The 260 GHz Martin-Pupplett EPR spectrometer operating on the DNP-NMR magnet was used to characterise the paramagnetic species used as polarising agents in the DNP experiments. Other promising systems, such as materials with conduction electrons and surface radicals in titanium dioxide, were also studied as prospective polarising agents for future experiments. The VDI Tx-237 source used for the EPR measurements has a wide frequency tuning range, from 245 GHz to 275 GHz and the spectrometer can, in principle, be operated in frequency-swept mode. However, as the propagation of microwaves in the spectrometer is quasi-optical, each horizontal surface and interface in the optical path gives rise to reflections. All of these reflected waves interfere at the detector, causing the EPR signal to be superposed by a ‘standing wave’ pattern, as in figure 4.1a. Isolating individual contributions and extracting the true EPR signal from such measurements is a highly subjective and time-consuming process. It is thus preferable to operate the spectrometer in fixed frequency mode. The resistive field sweep coil described in section 2.2 was used to perform these field-swept measurements. The coil, calibrated by performing 395 MHz ^1H NMR measurements, was found to have a field inhomogeneity of about 1 G, which is negligible for most high field EPR spectra.

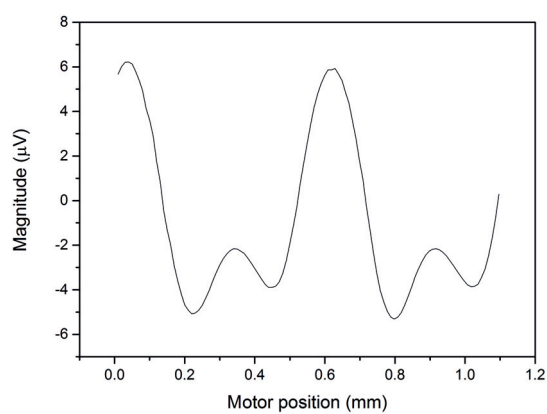
Due to the aforementioned standing waves, it is necessary to choose a frequency corresponding to constructive interference in order to maximise the signal intensity received. A frequency sweep is thus first performed around the expected resonance as in figure 4.1a and a maximum of the lock-in detected signal is chosen. As expected, choosing a frequency corresponding to a negative maximum of the detected signal results in an out of phase EPR spectrum (figure 4.1b). The position of the movable rooftop mirrors can be used to change the polarisation of microwaves used in the experiment. Figure 4.1c shows the variation of the field modulated signal detected by the lock-in amplifier as a function of the rooftop mirror position. As this measurement is performed at the EPR condition, the extrema correspond to Right Circular Polarisation, with Left Circular Polarisation theoretically occurring at zero detected signal. Linear Polarisation, which is what is used for the EPR measurements, lies in between. Thus, once the motor position has been set to Linear Polarisation, it is not normally necessary to adjust it for ordinary experiments.



(a) A frequency-swept measurement



(b) A field-swept measurement at the chosen frequency of 260.03 GHz



(c) A scan of the rooftop mirror position, controlling the incident beam polarisation

Figure 4.1 – A typical EPR measurement

4.1 EPR of Hyperpolarising Agents

4.1.1 TEMPOL in frozen solution

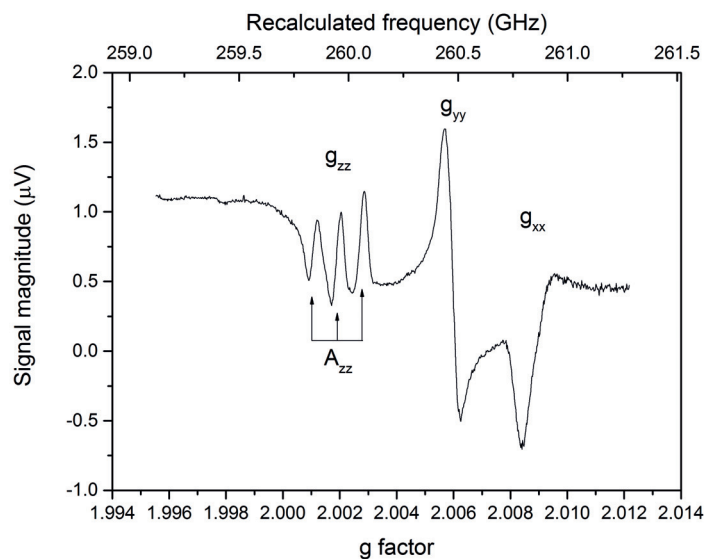
An EPR spectrum of the sample used in the cross effect DNP measurements in chapter 3 was measured using the Martin-Pupplet interferometer. The cryostat and probe were cooled slowly to 20 K and the sample was flash frozen outside the cryostat by dropwise addition into liquid nitrogen. The resulting glassy beads, of approximately 1.5 mm in diameter, were introduced into the cold cryostat and conveyed to the sample holder through a PTFE tube inserted into the hole in the sample holder seen in figure 2.13a. About 4.5 μ l of the sample thus prepared was used for the measurements. As TEMPOL is known to have an inhomogeneous EPR line of about 1 GHz in width at 9 T due to g-factor anisotropy, the measurement could not be performed with a single field sweep of the coil. Five overlapping field-swept measurements with widths of ± 100 G were performed at 259.4, 259.8, 260.2, 260.6 and 261 GHz. The field sweep range of each data set was transformed into a range of effective g-factors and the five datasets were scaled in amplitude to match the overlapping regions. The measurement at 260.2 GHz had to be horizontally scaled to 260.213 GHz, possibly as a result of experimental error. The resulting stitched EPR spectrum is shown in figure 4.2a. The integrated spectrum in figure 4.2b was obtained after baseline correction of this derivative spectrum.

The spin Hamiltonian parameters obtained by inspection from figure 4.2, $g_{XX} = 2.0080$, $g_{YY} = 2.0060$, $g_{ZZ} = 2.0022$, $A_{ZZ} = 100$ MHz, are similar to those reported in literature for TEMPOL [61]. Significant distortion is seen around the g_{ZZ} region of the integrated spectrum, and is an artefact of the stitching process. The integrated spectrum is highly sensitive to baseline drift, and while this can be corrected on a global scale by subtracting a suitable baseline function, drift in the individual measurements prior to stitching cannot be corrected in this manner. This results in local distortions within the resultant spectrum.

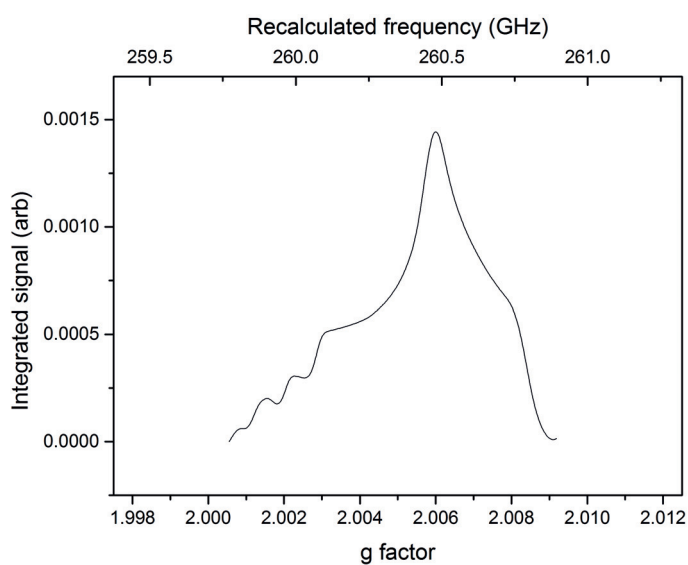
4.1.2 BDPA

BDPA, the free radical used in the Overhauser DNP experiments in liquid and in solid, is known to have an extremely narrow EPR line with a negligible g-factor anisotropy. Thus, for both the liquid and solid Overhauser experiments, it was necessary to precisely measure the BDPA EPR spectrum at the magnetic field used for DNP, in order to tune the gyrotron to high power operation at the required frequencies. A 5 mM solution of BDPA was prepared in toluene for the measurements. The small dipole moment of toluene as compared to water suggests that dielectric heating will be minimal, and the sample volume used was correspondingly larger, about 30 μ l. The X-band EPR measurement was performed on a 2 μ l sample.

As seen in figure 4.3, the peak-to-peak linewidth of the EPR spectrum remains the same (9 G or 25 MHz) at 9 GHz and at 260 GHz. This field independent broadening suggests that the linewidth is mainly due to unresolved hyperfine lines due to the 21 ^1H nuclear spins present on the molecule, as the hyperfine Hamiltonian terms do not depend on the external field. Can

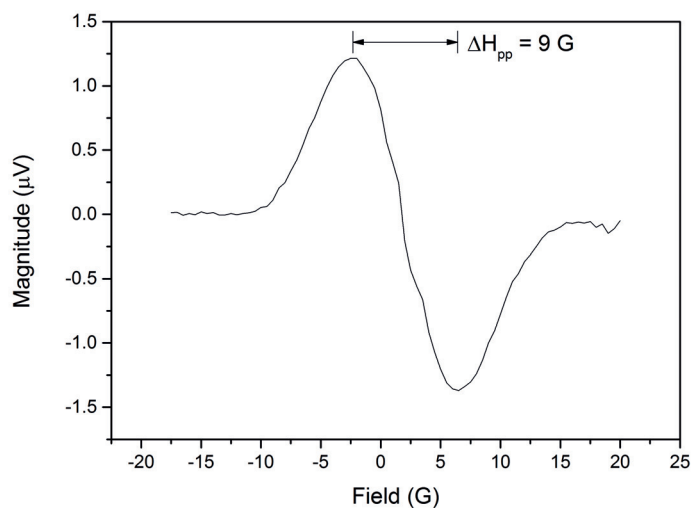


(a) The derivative EPR spectrum obtained from individual field-swept spectra, amplitude scaled and stitched

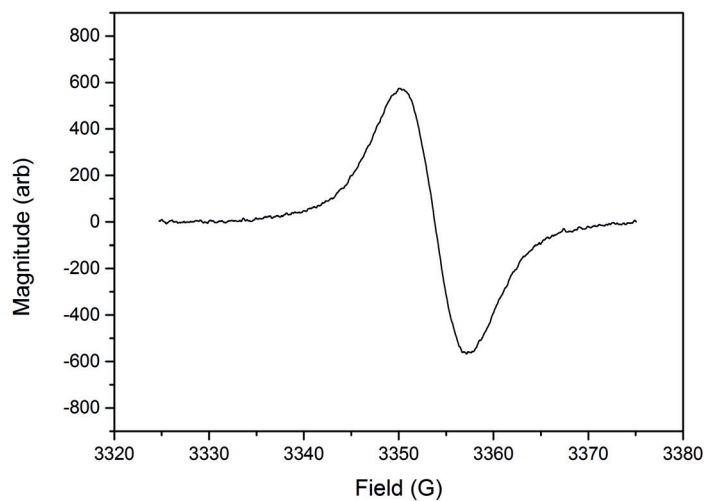


(b) Integrated EPR spectrum after baseline correction

Figure 4.2 – EPR spectrum of a frozen solution of 40 mM TEMPOL in 10 % protonated glycerol-water at 9.2775 T, at 20 K. The sample volume of 4.5 μl corresponds to about 10^{17} spins, and the spectra were acquired as single scans with a lock-in time constant of 1 s



(a) A field-swept EPR measurement of 5 mM BDPA in toluene at 259.993 GHz and 9.2765 T



(b) X-band (9.4313 GHz) EPR measurement of 5 mM BDPA in toluene

Figure 4.3 – High field and X-band solution EPR spectra of BDPA radicals in toluene at 300 K. The samples contain about 10^{17} and 10^{16} spins respectively, and the spectra were acquired as single scans

et al. report hyperfine lines from the ^1H spins in their X-band EPR measurement of $50\text{ }\mu\text{M}$ BDPA in toluene [53]. It is likely that dipolar broadening of the individual lines prevents us from observing them in figure 4.3a. However, as the sample was already at the limits of the spectrometer's sensitivity, a measurement at lower concentration could not be performed. The g-factor obtained from this measurement is 2.00221, which differs by $\Delta g = -0.0003$ from that in the polystyrene measurement below. Such a g-factor shift is not known from literature. Moreover, this value is also different from that seen in the ^{31}P liquid Overhauser DNP measurements in section 3.3.1, and is probably due to experimental error in calibrating the different frequency sources used. Further experiments need to be performed to isolate and correct for this source of error.

The sample used for Overhauser DNP in polystyrene was also measured in the Martin-Pupplett spectrometer, to compare the obtained enhancement profile with the EPR spectrum, and the data are shown in figure 4.4. The spectrum displays some asymmetry, and is centred around a g-factor of 2.00256.

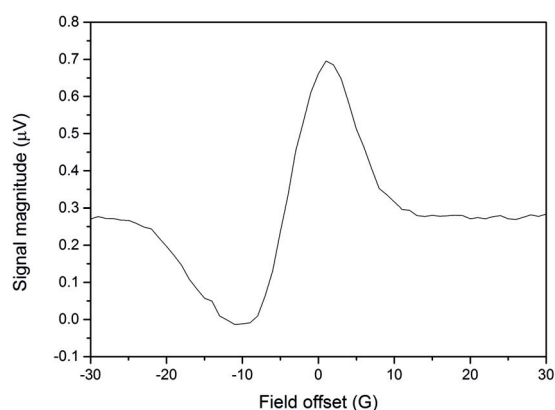
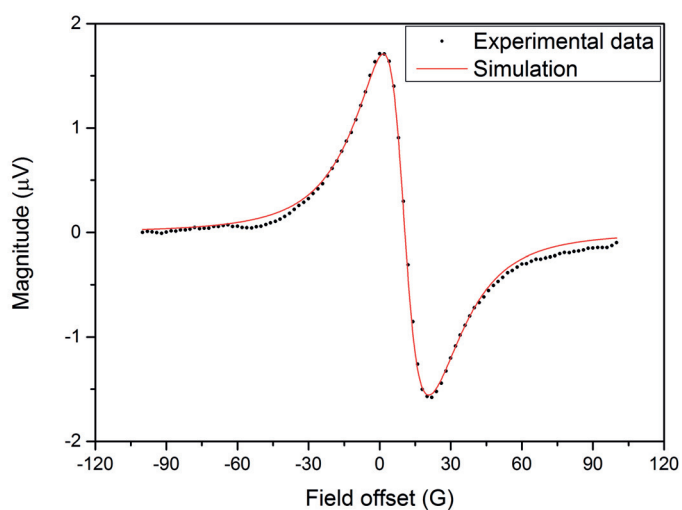


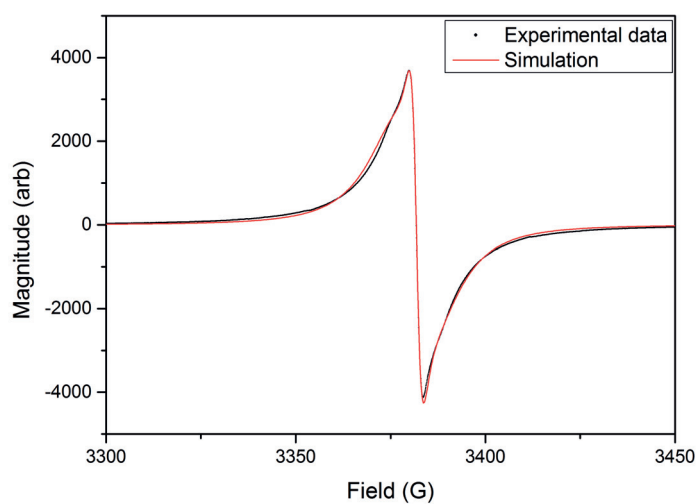
Figure 4.4 – EPR spectrum of BDPA in polystyrene at 260.0223 GHz, 9.2774 T and 300 K

4.1.3 Diamond nanopowder

The study of electronic and nuclear spins in diamond has seen considerable interest, especially for quantum information applications. Due to the rigidity of the diamond lattice, both nuclear spins and electronic spins in defect centres have very long relaxation times. Weak nuclear coupling to the lattice is also a desirable characteristic for DNP, as this reduces ‘leakage’ of the nuclear polarisation during the hyperpolarisation process. Moreover, diamond is known to be a biocompatible material, comparable to stainless steel or titanium [62]. This, combined with the potential for use as a polarising agent, makes diamond an attractive candidate for hyperpolarised imaging. ^{13}C DNP experiments performed at 3.35 T and in MAS conditions at 9 T by Bretschneider et al. on diamond nanopowders yielded significant enhancements between 100 and 300 [63]. They only observed these enhancements in samples of particle size



(a) High field EPR spectrum of the diamond nanopowders at 9.2942 T, 260.495 GHz and 150 K



(b) X-band EPR spectrum of the diamond nanopowder sample at 9.4797 GHz

Figure 4.5 – High field and X-band EPR spectra of the diamond sample. The red lines are simulated EPR spectra with the parameters in table 4.1

		g-factor	Linewidth (G)	Weight	RMSD
High field	Spin A	2.0023	12.948	1	0.0076
	Spin B	2.00226	26.208	6.1	
X-band	Spin A	2.00278	3.155	1	0.0098
	Spin B	2.00306	12.651	10.97	

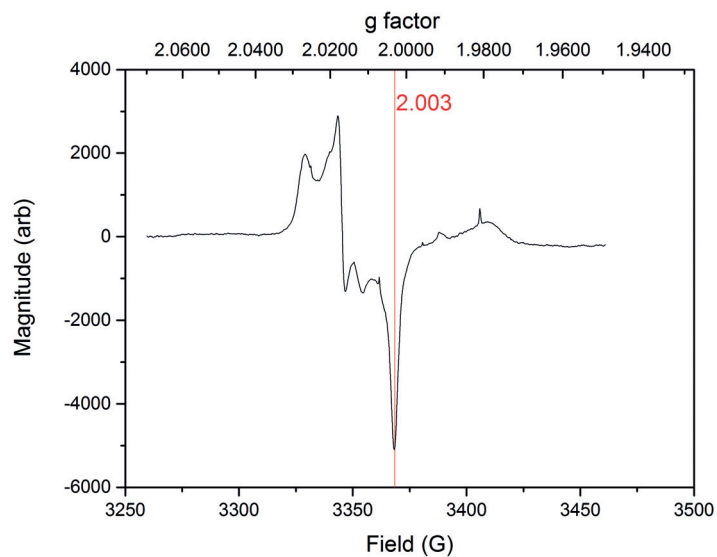
Table 4.1 – Spin Hamiltonian used to simulate the diamond EPR spectra

greater than 40 nm. The EPR spectra of the samples larger than 40 nm in size were dominated by P1 centres with strong hyperfine coupling to the adjacent ^{14}N nucleus. They did not see any DNP enhancement with the 10 nm samples and the EPR spectrum had a single featureless line attributed to surface defects. As our nanopowder samples have an intermediate average size of 20 nm, examining the EPR spectrum can provide insights into the DNP results observed.

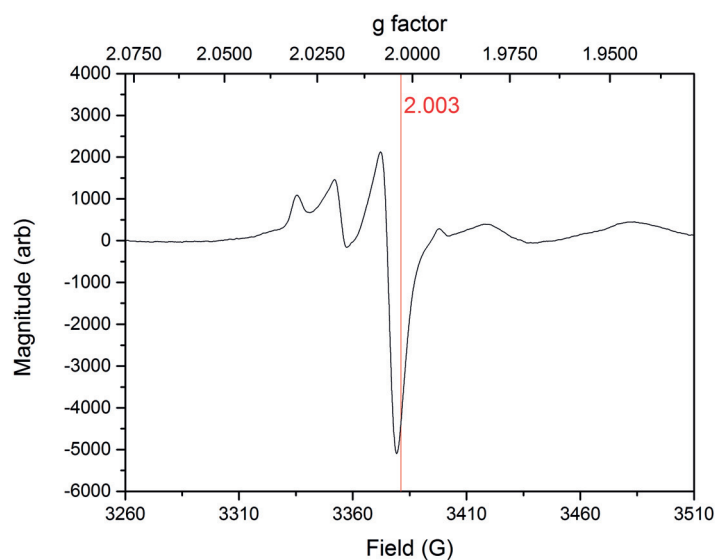
The EPR spectrum seen in figure 4.5a can be adequately fitted by the relatively simple systems consisting of two $S = 1/2$ spins given in table 4.1. The simulations and curve fitting were done using the EasySpin Matlab toolbox [64]. The large discrepancy between the g-factors obtained at 9 T and at X-band is likely due to the lack of an external reference in the X-band measurement, coupled with poor spectral resolution at 9 GHz. The linewidths at high field are 2-4 times larger than at X-band. As linewidths dominated by g-factor anisotropy would be 30 times larger at 9 T than at X-band, the spectra can be assumed to be homogeneously broadened. The narrow line at a g-factor of 2.0023 is similar to the P1 centres reported by Bretschneider et al., but the prominent ^{14}N hyperfine splitting observed in their larger samples is not seen. The broader line, while considerably shifted in position, is similar to that in their 10 nm samples, attributed to surface defects. These differences are likely due to different surface conditions in our samples and due to the high energy electron bombardment.

4.2 Paramagnetic Centres in Titanium Dioxide

Titanium dioxide is known to exhibit photocatalytic behaviour. Of the four recognised crystalline polymorphs of TiO_2 , rutile and anatase are the most common, and have tetragonal lattices. As the bandgap of rutile TiO_2 is 3.05 eV (about 406 nm) and that of anatase is usually 3.2 eV or higher (about 387 nm) [65], violet or ultraviolet irradiation is necessary to generate the radicals responsible for this catalytic behaviour. It has been observed that rutile and anatase do not display the same amount of photocatalytic activity: anatase has been found to be about 3 times more active than rutile [66]. However, a mixture of anatase and rutile in the ratio 3:1, commercially sold by Evonik Degussa as Aeroxide P25, is more active than either of the individual pure components [67]. EPR measurements of the radical species formed in commercial and surface modified TiO_2 were undertaken at X-band and at 9 T. It is known that spatial separation of the photogenerated electron-hole pairs occurs in TiO_2 , with the electrons migrating towards the bulk and holes migrating towards the surface [68]. Previous



(a) X-band EPR spectrum of Degussa P25 under UV irradiation at 9.4431 GHz



(b) X-band EPR spectrum of dehydrated Degussa P25 under UV irradiation at 9.4788 GHz

Figure 4.6 – X-band EPR spectra of the UV excited Degussa P25 samples at 77 K before and after dehydration

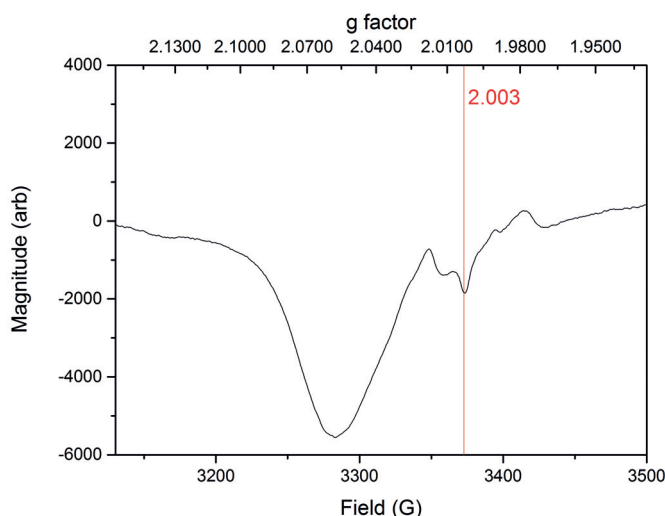


Figure 4.7 – X-band EPR spectrum of phosphoric acid functionalised Degussa P25 under UV irradiation at 9.4552 GHz at 77 K

reports have assigned the surface radicals to hydroxide (OH^\bullet) and superoxide ($\text{O}_2^{\bullet-}$) species, probably formed by the reaction of photogenerated electron-hole pairs with surface bound hydroxyl groups and water, as well as to $\text{O}^{\bullet-}$ groups formed by the interaction of holes with oxide of the crystal lattice near the surface [69, 70].

Degussa P25 powder, purchased from Sigma-Aldrich, was dehydrated by heating at 250 °C for 30 min in a nitrogen environment and the EPR spectrum of this sample was measured alongside the as-purchased powder. A 450 mW LED bank (LEDMOD V2 from Omicron-Laserage Laserprodukte GmbH) providing UV light at 365 nm was used to excite the TiO_2 samples for these measurements.

The obtained EPR spectra in figures 4.6a and 4.6b are fairly complex but match the specific features at g-factors of 2.003, 2.009 and 2.025 attributed to $\text{O}_2^{\bullet-}$ by Howe and Grätzel for measurements performed in an oxygen atmosphere [68]. The dehydrated samples show changes in the spectrum around 2.01 confirming that the species are formed at the surface. However, as the samples were re-exposed to the atmosphere after treatment, it is not possible to distinguish between the effects of bound hydroxyl species and changes in spatial distribution of the radicals due to desorption and resorption of oxygen. Unexpectedly, these features observed in the as-purchased powder most resemble the spectra obtained by Nakaoka and Nosaka in anatase heated to 700 °C for 5 h before UV illumination [70].

TiO_2 functionalised by phosphoric acid has been shown to exhibit reduced photocatalytic activity [71]. This effect is likely due to the phosphoric acid bonding to titanium sites on the surface, effectively acting as a passivating layer against the formation of surface radicals. To study this, the dehydrated sample as prepared before was suspended in a solution of 2 M phosphoric acid in water for 12 h. The resulting suspension was separated by centrifugation,

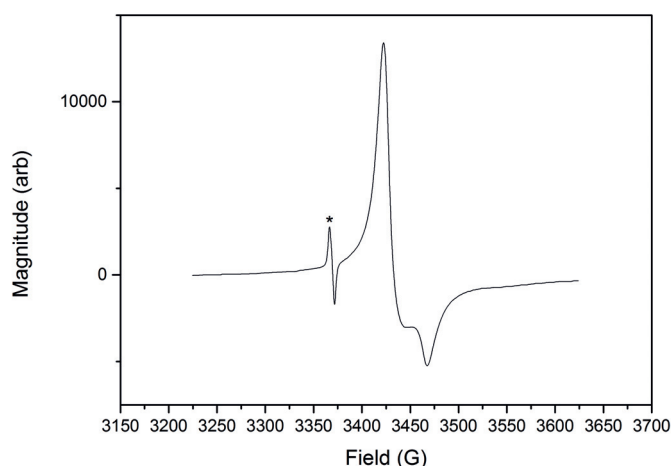


Figure 4.8 – X-band EPR spectrum of surface radicals in Degussa P25 heated to 700 °C for 4 h, at 9.445 78 GHz. DPPH used as a reference is marked with an asterisk at $g = 2.0036$

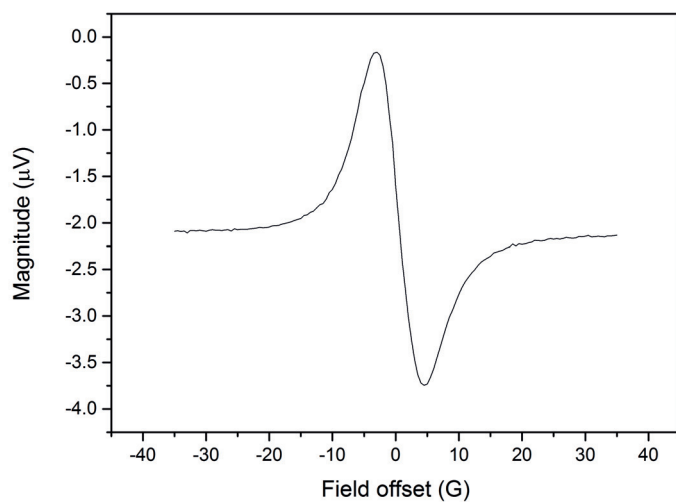
and the nanopowder was washed and dried at 200 °C. The sample was kept away from light sources for the entire duration of sample preparation until the measurements were performed, to avoid any light catalysed degradation of the phosphoric acid layer. As the band gap of the rutile phase falls within visible light range, ambient light sources might be sufficient to cause photocatalysis. The EPR spectrum of this functionalised TiO_2 sample was then measured under UV irradiation.

In the obtained EPR spectrum, shown in figure 4.7, the prominent narrow features at a g -factor of 2 seen in figures 4.6a and 4.6b are almost completely suppressed. This suggests that the radicals observed are not $\text{O}^{\bullet-}$ due to holes trapped at lattice oxide sites, as these sites are unaffected by phosphoric acid functionalisation. A broad EPR line with a higher g -factor of about 2.07, not seen in the non-functionalised samples, dominates the spectrum. Interestingly, the features at 1.99 and 1.98 appear unchanged in amplitude and shape in the EPR spectra of all three samples above, indicating that they do not arise from the surface. Their positions are similar to that reported by Howe and Grätzel for trapped electrons in bulk Ti_3^+ sites [68].

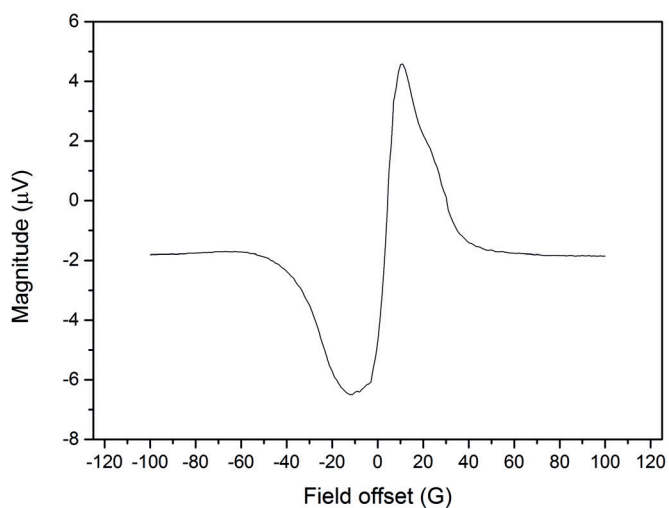
It has been shown that TiO_2 , when reduced at high temperatures in an atmosphere of hydrogen, also has surface radicals corresponding to Ti_3^+ , which are stable when stored in an inert environment. Further, the paramagnetic species obtained in rutile and in anatase powders treated in this manner have different g -factors, and the rutile is seen to more readily reduce than anatase [72]. In order to study this effect, P25 powders were heated in a furnace in an atmosphere of 5 % hydrogen and 95 % argon, purchased as ARCAL 15 from Carbogas (Air Liquide), at 700 °C for 4 h and sealed in a 5 mm commercial NMR tube. The EPR spectrum of this sample was measured at 77 K at X-band.

4.3 Conducting Polymers

Conductive behaviour has been observed in organic polymers in pellet and film form since the 1960s. In polymers where conduction is primarily due to polarons, the conduction electron spin resonance (CESR) of these charge carriers can be studied to provide insights into carrier transport [73]. Polyaniline in its emeraldine form shows a transition from insulating to conductive behaviour as it is protonated [74]. This protonation is achieved by treating the emeraldine base (PANI-EB) form with an acid, resulting in varying proportions of the protonated and conducting emeraldine salt (PANI-ES) form. High-field EPR measurements were performed at room temperature on PANI-ES and PANI-EB, purchased from Sigma-Aldrich, and two distinct EPR lineshapes were observed for the insulating and the conducting material respectively (figure 4.9). The EPR spectrum of PANI-ES is a featureless, narrow line with a peak-to-peak linewidth of 8 to 10 G, while the PANI-EB spectrum seems to be dominated by a much broader component superimposed on a narrow line. As the degree of protonation and the nature of the acid used during synthesis was not known, further study and analysis was not performed.



(a) An EPR measurement on the conducting, emeraldine salt of polyaniline (PANI-ES) at 260.046 GHz



(b) An EPR measurement on the insulating, emeraldine base of polyaniline (PANI-EB) at 260.048 GHz

Figure 4.9 – High field EPR measurements of the salt and base variants of polyaniline at 9.277 T and 300 K. The narrow line in PANI-ES is likely due to the mobility of the charge carriers

Conclusion and Future Prospects

A brief summary of the experimental results presented in the thesis is gathered below. Further experiments that would complement the existing measurements but that were not undertaken during the course of this project are also discussed. In particular, the expected installation of a new cryogen-free magnet system with field sweep coils in the months immediately following the presentation of this thesis opens up new possibilities for high field EPR measurements that were not possible due to limitations in the current setup.

DNP experiments

Successful cross effect DNP was demonstrated on frozen solutions of the monoradical TEM-POL in a solution of 60 % d8-glycerol, 30 % D₂O and 10 % H₂O by volume. The ¹H NMR signals were shown to be enhanced by a factor of up to 40 with respect to the thermal equilibrium value under monochromatic irradiation of microwaves. As our experiments are performed in static conditions, we do not obtain the large enhancement values reported in literature under Magic Angle Spinning. The DNP measurements were performed in a range of temperatures from 20 K to 100 K using the gyrotron as microwave source. The fast switchability of the gyrotron was exploited to reduce microwave heating, by switching off the output during a 'cooling time' between acquisition cycles. The frequency tunability of the gyrotron enabled us to record a partial measurement of the enhancement as a function of frequency of irradiation. At 20 K, the microwave power required was low enough that a solid state source, the VDI Tx-237 from Virginia Diodes, could be used in place of the gyrotron. Using this source, a complete frequency profile of the enhancement was obtained, which matched theoretical expectations and past reports in literature.

The flexibility in frequency control of the gyrotron was demonstrated by acquiring cross effect DNP-NMR spectra while rapidly modulating the microwave frequency. A gain in enhancement of up to 70 % was obtained at 20 K with a modulation depth of ± 50 MHz at a rate of 2 kHz. This increased to 80 % at 70 K, but faster modulation of up to 13 kHz was necessary. A more detailed study of this was undertaken at 20 K with the VDI source, and an optimum modulation depth of ± 120 MHz was found, with a gain in enhancement of about 100 %.

In order to manage the dielectric heating produced by the gyrotron output at high powers,

Conclusion and Future Prospects

a planar probe design was tested at both 300 K and low temperature. High powers were necessary to observe DNP through the Overhauser effect in liquids and solids, or through the solid effect in solids. Samples of 80 mM TEMPOL dissolved in H₂O were used as a probe for ¹H Overhauser DNP in liquids. The gyrotron was used to provide 70 W of power at the EPR resonance frequency of TEMPOL, and an enhancement of -14 was observed at 300 K, consistent with prior reports in this system. The improvement we bring to this technique is the ability to work with larger sample volumes than reported before, and contrary to previous experiments, the planar probe frees us from active cooling. ³¹P Overhauser DNP was observed in a solution of 1 M triphenyl phosphine in fluorobenzene, using 80 mM BDPA as polarising agent. The dependence of the enhancement on microwave power, from 1 to 20 W was measured, and a maximum positive enhancement of 200 was seen.

The planar probe was also used at low temperatures, down to 20 K, in solid samples. The Overhauser effect was observed in a 90 % deuterated polystyrene matrix with 2 % by weight of BDPA as a function of sample temperature. A maximum positive enhancement of 16 was observed, with 4.5 W of power, at 20 K. The frequency dependence of the enhancement was also measured at 20 K, which matched the EPR spectrum of BDPA in this system. ¹³C solid effect measurements on diamond nanopowder yielded a maximum enhancement of about 30 at 20 K. Saturation of the enhancement was not observed even with 60 W of circularly polarised microwave power.

The performance of the Matching Optics Unit for polarisation control of the gyrotron output was tested by a Schottky diode detector as well as cross effect DNP. Circular polarisation, with some visible distortion, was verified after reflection from the miter bend, attesting to the quality of transmission achieved with SwissTo12's corrugated waveguides. The DNP enhancement was also seen to be improved by about 70 % at low microwave power with right circular polarisation. The MOU was used to increase the effective power in the ¹H liquid Overhauser effect experiments as well as in the solid effect experiments.

Future NMR experiments

1 Surfaces

The gyrotron DNP setup can be used for surface NMR measurements of the titanium dioxide samples studied in chapter 4. Through cross effect DNP and possibly cross polarisation, surface titanium and oxygen sites on these catalysts can be explored. Preliminary DNP experiments on a TiO₂ sample wet with a solution of TEMPOL yielded moderate ¹H enhancements, indicating that the TiO₂ allows enough microwave penetration for DNP. Double resonance experiments without DNP could also be used to study the samples that were surface functionalised with phosphoric acid. A preliminary ³¹P NMR measurement of such a sample at room temperature yielded a large signal but no DNP enhancement. NMR of this sample under UV irradiation will complement the EPR measurements performed, and help characterise catalysis in this system.

Molecules grafted onto the diamond nanopowder can serve as probes for polarisation transfer through the solid effect external to the nanoparticle itself.

2 Mechanistic studies

The mechanism of the cross effect in monoradical systems and static conditions needs to be studied in more detail. The parameter space of modulation amplitude and rate, in the frequency modulated DNP experiments can be explored more completely in analogy to similar studies at 3 T [49]. The frequency profile of the enhancement has also been reported to change under frequency modulation at lower fields, and is worth examining at 9 T as well.

Integrating the sweep coil used for EPR with the planar probe used for high power DNP will allow the measurement of enhancement maps for the solid effect and Overhauser effect. A comparison of these enhancement maps with the EPR signals measured as a function of temperature is invaluable for the diamond nanopowder samples, and can be used to isolate solid effect contributions from bulk and surface paramagnetic centres.

EPR

The home build Martin-Pupplett EPR spectrometer was successfully used to measure EPR spectra of paramagnetic centres used for DNP in both liquid and solid samples. A stitched EPR spectrum of the frozen solution of TEMPOL used for cross effect DNP was recorded, which matched well with literature reports and the DNP enhancement. EPR measurements on the diamond nanopowder samples showed significant differences as compared to X-band data, and were used to precisely find the microwave irradiation frequency for DNP. Similarly, the g-factor of BDPA used for Overhauser DNP in the solid sample as well as the liquid sample was found by a high field EPR measurement of BDPA in polystyrene. A measurement on the conductive polymer polyaniline in its emeraldine salt and base forms yielded interesting EPR data, which could not be analysed further as the exact chemical composition was unknown.

X-band EPR measurements of paramagnetic centres in commercial nanopowders of titanium dioxide, manufactured by Degussa, were performed under different conditions and surface treatment. UV irradiated EPR of as purchased, dehydrated, and phosphoric acid functionalised titanium dioxide was studied. Qualitative differences in the surface paramagnetic species produced in each case were observed. As purchased titanium dioxide was also treated with hydrogen gas at 400 °C to partially reduce the surface, resulting in an EPR spectrum that was shifted to much lower g-factors than in the above cases. Thus, this preliminary observation suggests the possibility of studying g-shifts in EPR to characterise chemisorption.

Conclusion and Future Prospects

Future experiments

The use of a wide range field sweep coil will considerably supplement the capabilities of the current high field EPR spectrometer. More accurate, artefact free EPR spectra of the frozen TEMPOL sample need to be measured. These can be used together with measurements of the DNP enhancement profile at different monoradical concentrations to obtain a better understanding of the observed DNP mechanism.

The titanium dioxide samples measured at X-band all show extremely large lines broadened by g-factor anisotropy, which will be measurable with such a field sweep coil.

Measurement of conduction electron spin resonance in metallic films is possible in our system due to the geometry of the spectrometer, and is an interesting field to explore.

A NMR of Functionalised TiO₂

The purpose of this appendix is to document the preliminary NMR and DNP measurements performed on functionalised TiO₂. As the experiments do not discriminate between surface species and those in the bulk, these are not truly surface NMR data. However, these experiments can serve to guide future endeavours to measure properties of surface species in such samples. Two proof of concept cross effect DNP measurements are also presented to demonstrate that TiO₂ in this form permits sufficient microwave transmission for DNP.

A.1 Formic acid functionalised TiO₂

About 40 mg of Degussa P25 was heated in a nitrogen environment at 200 °C for one hour to remove surface water. This dehydrated powder was suspended in 4 ml of 1 M 99 % ¹³C enriched formic acid solution in water. The suspension was separated in an ultrasonic bath for 1.5 h, and left to stand overnight. The sample was then dried and about 43 mg of the dried powder was recovered and measured at 300 K in the NMR spectrometer. The sample was maintained in the dark throughout this procedure, to prevent UV excitation and possible photocatalysis. The ¹³C NMR spectrum obtained from a solid echo at 40 μs is shown in figure A.1.

The NMR line, centred at -70 ppm, has the same chemical shift as neat formic acid measured at this frequency. The linewidth of 23 ppm is marginally larger than that of neat formic acid measured in our spectrometer, which is 15 ppm. The carboxyl group of formic acid is expected to bind to titanium sites on TiO₂ and hence, the chemisorbed compound is not expected to be acidic. However, as evidenced by the relatively narrow linewidth of the NMR spectrum, the majority of the formic acid in this sample is mobile, and can be expected to quench nitroxide radicals upon contact. Indeed, negligible cross effect DNP enhancement was seen when this sample was wet with 40 μl of TEMPOL dissolved in D₂O, frozen to 20 K and irradiated with microwaves.

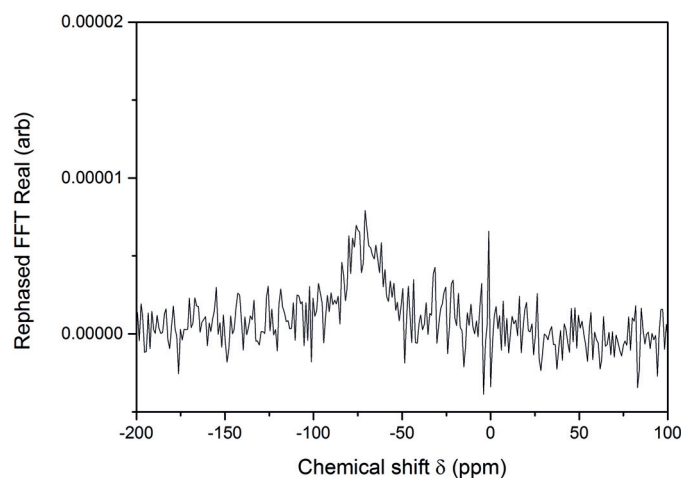


Figure A.1 – ¹³C NMR spectrum obtained from a solid echo sequence on TiO₂ functionalised with formic acid at 300 K, $\omega_n = 99.3309$ MHz

A.2 Phosphoric acid functionalised TiO₂

About 70 mg of Degussa P25 was functionalised with phosphoric acid using the method used for EPR measurements as described in section 4.2. As above, the sample was kept in the dark, and the ³¹P NMR was measured at 300 K, as shown in figure A.2. The sample was mixed with a solution of 40 mM TEMPOL in 60 %/40 % glycerol/water to perform direct ³¹P DNP, but no DNP enhancement was seen with this sample.

Two distinct peaks are seen in the NMR spectrum, a narrow line at 0 ppm and a broad line at +73 ppm. However, saturation recovery measurements on this sample could only be fit by assuming biexponential recovery functions for both peaks. Moreover, the fits for the two peaks shared a common time constant of 23 s. This strongly indicates the presence of a third, superimposed NMR line in the measured spectrum and indeed, fitting of the spectrum to three components produced better results than to two. The most optimum fit yielded a Lorentzian line with a FWHM of 5.6 ppm for the peak at 0 ppm, a Lorentzian with a FWHM of 37.8 ppm for the peak at +73 ppm, and a Gaussian with a FWHM of 77.9 ppm centred at +18 ppm. Fitting the saturation recovery data to these three lines yielded monoexponential fits for all three peaks, with T_1 values of 1.5 s, 5 s and 23 s for the peaks at 0, +73 and +18 ppm respectively.

The narrow peak at 0 ppm indicates that the sample contains a lot of mobile phosphoric acid, and that the washing procedure was not sufficient to remove all excess acid. This also explains the feature at +73 ppm, which is possibly a result of a reaction between the mobile phosphoric acid and the glycerol and TEMPOL solution. This also explains the lack of DNP enhancement seen as the TEMPOL would have degraded in the acidic environment.

A second sample of phosphoric acid functionalised TiO₂ was prepared using the same pro-

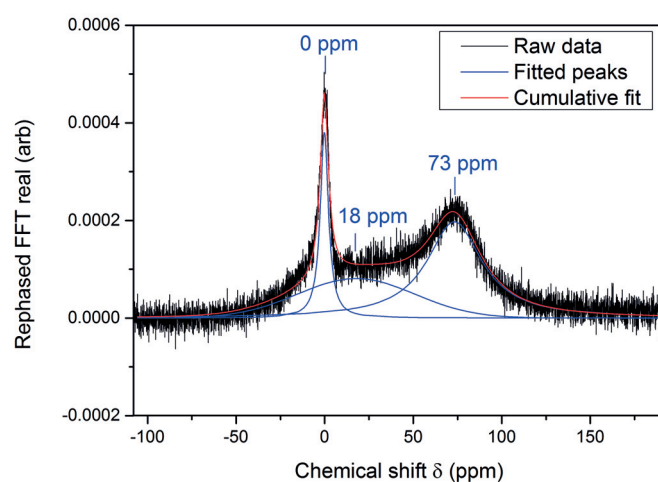


Figure A.2 – ^{31}P NMR spectrum obtained from an FID on TiO_2 functionalised with phosphoric acid at 300 K, $\omega_n = 159.882$ MHz

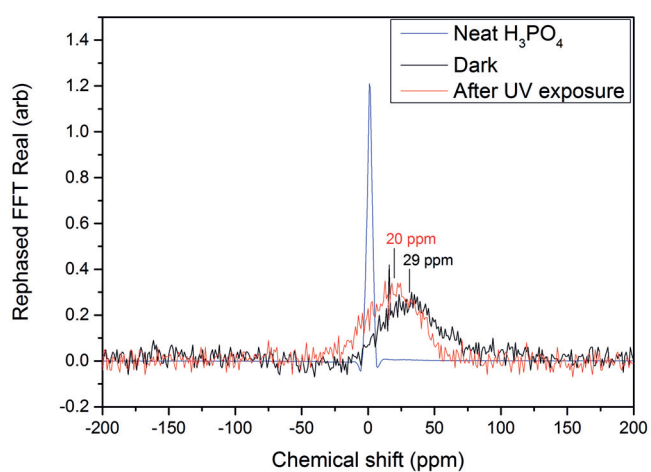


Figure A.3 – ^{31}P NMR spectrum obtained from an FID on TiO_2 functionalised with phosphoric acid at 300 K, $\omega_n = 157.6$ MHz

cedure described above, and this sample was washed and centrifugated 5 times. ³¹P NMR of the resulting powder, without any additional glycerol or TEMPOL, was measured at room temperature. Figure A.3 shows the NMR spectrum of this sample, with the signal from a separate sample of neat phosphoric acid superimposed as reference. A single peak at +20 ppm is seen, corresponding to the hidden peak in figure A.2 - the other two peaks due to mobile phosphoric acid are not seen. This indicates that the washing procedure in this sample was successful. DNP was not attempted with this sample.

A.3 Cross effect ¹H DNP on TiO₂

TiO₂ powders are known to contain large amounts of adsorbed water. 20 mg of as purchased Degussa P25 was wet with 20 µl D₂O containing 40 mM of TEMPOL. This sample was frozen at 20 K and ¹H DNP-NMR was obtained. An enhancement of about 19 was observed at the cross effect condition, demonstrating that DNP in samples containing TiO₂ is viable. A second measurement was performed after dehydrating the Degussa P25 powder in a nitrogen environment at 200 °C for one hour to remove physisorbed water. The resultant powder had a much reduced remnant ¹H NMR signal. Wetting with the above solution of TEMPOL in D₂O yielded a ¹H DNP enhancement of only 2. When the TEMPOL solution was prepared with d8-glycerol instead of D₂O, a much improved enhancement of about 10 was seen (figure A.4).

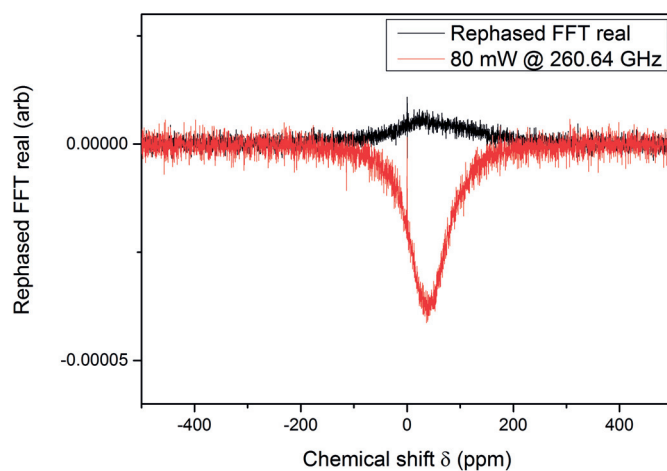


Figure A.4 – ¹H NMR spectra with and without microwaves obtained with a FID of dehydrated TiO₂ at 20 K with TEMPOL dissolved in d8-glycerol

B Optically Pumped Hyperpolarisation in InP

This appendix outlines experimental data acquired and published during the first few months of my PhD project, carrying over from experiments performed in my Master's project at the LPMN. Hyperpolarisation of ^{31}P nuclei was achieved by optical pumping (OPNMR) of compensated indium phosphide, doped with iron [75].

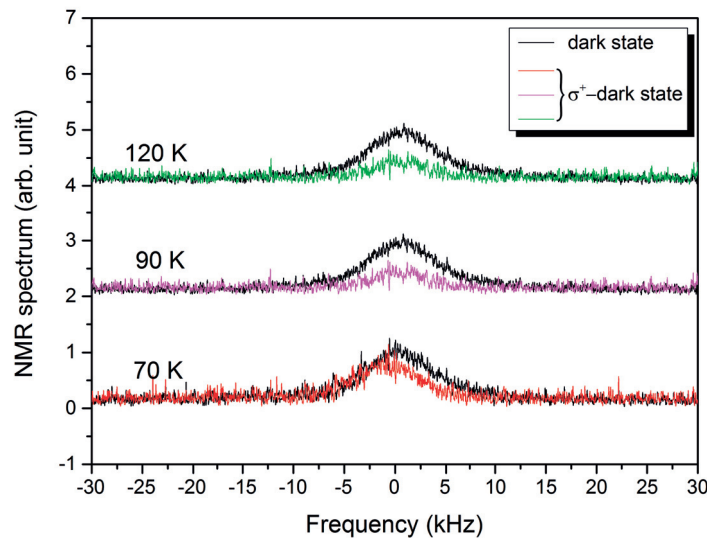


Figure B.1 – ^{31}P NMR spectra of InP:Fe, in the dark (black) and the differential signal observed in the presence of σ^+ light (coloured), showing signal enhancement with respect to the dark state

Optical pumping of semiconductors with circularly polarised light results in high electronic spin polarisation in the conduction band. Due to angular momentum selection rules, electrons of one spin are preferentially excited from the valence band, initially full, to the conduction band, initially empty. This results in a large population of highly mobile, spin polarised electrons in the conduction band. Similar to the Overhauser effect, these electrons

Appendix B. Optically Pumped Hyperpolarisation in InP

then undergo cross-relaxation with nuclei, producing hyperpolarisation, with the sign of the enhancement depending on light helicity. This has been reported in the literature for III-V semiconductors such as gallium arsenide [76] as well as indium phosphide [77]. Tycko, in [78], suggests the possibility of grafting biomolecules onto the surface of InP substrates and transferring this nuclear hyperpolarisation across the surface to these functionalised species, enhancing their NMR sensitivity.

As the growth process of indium phosphide results in natural n-doping, iron doped indium phosphide was used to obtain a compensated state of the semiconductor. 830 nm laser light at a power of 1 W was used in the experiment, and an optical fibre patch cable was introduced into the cryostat with linear and circular polarisers coupled to the end at the sample position, to ensure that the correct light polarisation reached the sample. ^{31}P NMR was measured using a single pulse FID measurement following a saturation comb, as in the experiments in chapter 3. However, as the T_{1n} is extremely long, about 900 s at 200 K but approaching 10 000 s at 10 K, the signal was obtained after only a partial recovery as a compromise between signal intensity and experimental time. The resulting spectra are shown in figure B.1 as a comparison between the dark state (black lines) and the signal obtained by taking the difference between the spectra with and without light (coloured lines). The enhancement thus obtained is underestimated by a factor of about 350, as the penetration depth of light is only 1 μm while the thickness of the wafer is about 350 μm . Moreover, it was found that the hyperpolarised nuclei have a much shorter polarisation build-up time T_b than the T_{1n} of the bulk, thermal nuclei. Thus, while the dark spectra represent partial saturation recovery, the spectra under irradiation have mixed contributions from fully recovered signals of the hyperpolarised nuclei and partially recovered signals of the bulk nuclei. Taking these two factors into account, the enhancement at 70 K was estimated to be about 35.

Bibliography

- [1] A. W. Overhauser, *Physical Review* **92**, 411 (1953).
- [2] R. A. Wind, F. E. Anthonio, M. J. Duijvestijn, J. Smidt, J. Trommel, and G. M. C. d. Vette, *Journal of Magnetic Resonance* (1969) **52**, 424 (1983).
- [3] T. Maly, D. Cui, R. G. Griffin, and A.-F. Miller, *The Journal of Physical Chemistry B* **116**, 7055 (2012).
- [4] B. D. Armstrong, J. Choi, C. López, D. A. Wesener, W. Hubbell, S. Cavagnero, and S. Han, *Journal of the American Chemical Society* **133**, 5987 (2011).
- [5] J. H. Ortony, B. Qiao, C. J. Newcomb, T. J. Keller, L. C. Palmer, E. Deiss-Yehiely, M. Olvera de la Cruz, S. Han, and S. I. Stupp, *Journal of the American Chemical Society* **139**, 8915 (2017).
- [6] M. C. Cassidy, H. R. Chan, B. D. Ross, P. K. Bhattacharya, and C. M. Marcus, *Nature Nanotechnology* **8**, 363 (2013).
- [7] G. Kwiatkowski, F. Jähnig, J. Steinhäuser, P. Wespi, M. Ernst, and S. Kozerke, *Scientific Reports* **7**, 7946 (2017).
- [8] J. H. Ardenkjær-Larsen, B. Fridlund, A. Gram, G. Hansson, L. Hansson, M. H. Lerche, R. Servin, M. Thaning, and K. Golman, *Proceedings of the National Academy of Sciences* **100**, 10158 (2003).
- [9] A. Bornet, R. Melzi, A. J. Perez Linde, P. Hautle, B. van den Brandt, S. Jannin, and G. Bodenhausen, *The Journal of Physical Chemistry Letters* **4**, 111 (2013).
- [10] L. R. Becerra, G. J. Gerfen, B. F. Bellew, J. A. Bryant, D. A. Hall, S. J. Inati, R. T. Weber, S. Un, T. F. Prisner, A. E. McDermott, et al., *Journal of Magnetic Resonance, Series A* **117**, 28 (1995).
- [11] V. Bajaj, C. Farrar, M. Hornstein, I. Mastovsky, J. Viereg, J. Bryant, B. Eléna, K. Kreischer, R. Temkin, and R. Griffin, *Journal of Magnetic Resonance* **160**, 85 (2003).
- [12] S. E. Shore, J.-P. Ansermet, C. P. Slichter, and J. H. Sinfelt, *Phys. Rev. Lett.* **58**, 953 (1987).
- [13] P.-K. Wang, J.-P. Ansermet, C. P. Slichter, and J. H. Sinfelt, *Phys. Rev. Lett.* **55**, 2731 (1985).
- [14] P.-A. Vuissoz, J.-P. Ansermet, and A. Wieckowski, *Phys. Rev. Lett.* **83**, 2457 (1999).

Bibliography

- [15] C. Caspers, P. F. da Silva, M. Soundararajan, M. A. Haider, and J.-P. Ansermet, *APL Photonics* **1**, 026101 (2016).
- [16] A. J. Rossini, A. Zagdoun, M. Lelli, A. Lesage, C. Copéret, and L. Emsley, *Accounts of Chemical Research* **46**, 1942 (2013).
- [17] F. A. Perras, Z. Wang, P. Naik, I. I. Slowing, and M. Pruski, *Angewandte Chemie International Edition* **56**, 9165 (2017).
- [18] A. Lund, M.-F. Hsieh, T.-A. Siaw, and S.-I. Han, *Physical Chemistry Chemical Physics* **17**, 25449 (2015).
- [19] T. Kobayashi, F. A. Perras, T. W. Goh, T. L. Metz, W. Huang, and M. Pruski, *The Journal of Physical Chemistry Letters* **7**, 2322 (2016).
- [20] M. T. Colvin, R. Silvers, Q. Z. Ni, T. V. Can, I. Sergeyev, M. Rosay, K. J. Donovan, B. Michael, J. Wall, S. Linse, and R. G. Griffin, *Journal of the American Chemical Society* **138**, 9663 (2016).
- [21] T. Kobayashi, I. I. Slowing, and M. Pruski, *The Journal of Physical Chemistry C* **121**, 24687 (2017).
- [22] I. Solomon, *Physical Review* **99**, 559 (1955).
- [23] A. Abragam, *Physical Review* **98**, 1729 (1955).
- [24] W. T. Wenckebach, *Essentials of dynamic nuclear polarization* (Spindrift Publications, The Netherlands, 2016).
- [25] C. P. Slichter, *Principles of magnetic resonance*, 3rd ed., Vol. 1, Springer Series in Solid-State Sciences (Springer-Verlag, 1990).
- [26] C. D. Jeffries, *Phys. Rev.* **106**, 164 (1957).
- [27] K. R. Thurber and R. Tycko, *Israel Journal of Chemistry* **54**, 39 (2014).
- [28] K.-N. Hu, G. T. Debelouchina, A. A. Smith, and R. G. Griffin, *The Journal of Chemical Physics* **134**, 125105 (2011).
- [29] E. J. de Rijk, 'Terahertz passive components for dynamic nuclear polarization nuclear magnetic resonance applications', doi:10.5075/epfl-thesis-6023, PhD thesis (École polytechnique fédérale de Lausanne, 2013), 144 pp.
- [30] E. de Rijk, A. Macor, J.-P. Hogge, S. Alberti, and J.-P. Ansermet, *Review of Scientific Instruments* **82**, 066102 (2011).
- [31] A. Abragam and M. Goldman, *Reports on Progress in Physics* **41**, 395 (1978).
- [32] S. Alberti, J.-P. Ansermet, K. A. Avramides, F. Braunmueller, P. Cuanillon, J. Dubray, D. Fasel, J.-P. Hogge, A. Macor, E. d. Rijk, M. d. Silva, M. Q. Tran, T. M. Tran, and Q. Vuillemin, *Physics of Plasmas* **19**, 123102 (2012).
- [33] A. Henstra, P. Dirksen, and W. T. Wenckebach, *Physics Letters A* **134**, 134 (1988).
- [34] A. Henstra and W. Wenckebach, *Molecular Physics* **112**, 1761 (2014).

-
- [35] C.-G. Joo, K.-N. Hu, J. A. Bryant, and R. G. Griffin, *Journal of the American Chemical Society* **128**, 9428 (2006).
- [36] D. Yoon, M. Soundararajan, C. Caspers, F. Braunmueller, J. Genoud, S. Alberti, and J.-P. Ansermet, *Journal of Magnetic Resonance* **270**, 142 (2016).
- [37] A. Macor, E. de Rijk, S. Alberti, A. Comment, and J.-P. Ansermet, in 2011 international conference on infrared, millimeter, and terahertz waves (Oct. 2011), pp. 1–2.
- [38] J. W. Lamb, *International Journal of Infrared and Millimeter Waves* **17**, 1997 (1996).
- [39] A. K. Jonscher, *Journal of Physics D: Applied Physics* **32**, R57 (1999).
- [40] B. D. Armstrong, D. T. Edwards, R. J. Wylde, S. A. Walker, and S. Han, *Physical Chemistry Chemical Physics* **12**, 5920 (2010).
- [41] K. R. Thurber, W.-M. Yau, and R. Tycko, *Journal of Magnetic Resonance* **204**, 303 (2010).
- [42] C. Song, K.-N. Hu, C.-G. Joo, T. M. Swager, and R. G. Griffin, *Journal of the American Chemical Society* **128**, 11385 (2006).
- [43] C. Sauvé, M. Rosay, G. Casano, F. Aussenac, R. T. Weber, O. Ouari, and P. Tordo, *Angewandte Chemie* **125**, 11058 (2013).
- [44] K. R. Thurber and R. Tycko, *The Journal of Chemical Physics* **140**, 184201 (2014).
- [45] F. Mentink-Vigier, S. Paul, D. Lee, A. Feintuch, S. Hediger, S. Vega, and G. De Paëpe, *Physical Chemistry Chemical Physics* **17**, 21824 (2015).
- [46] F. Mentink-Vigier, Ü. Akbey, H. Oschkinat, S. Vega, and A. Feintuch, *Journal of Magnetic Resonance* **258**, 102 (2015).
- [47] A. Baudot, L. Alger, and P. Boutron, *Cryobiology* **40**, 151 (2000).
- [48] A. Bornet, J. Milani, B. Vuichoud, A. J. Perez Linde, G. Bodenhausen, and S. Jannin, *Chemical Physics Letters* **602**, 63 (2014).
- [49] Y. Hovav, A. Feintuch, S. Vega, and D. Goldfarb, *Journal of Magnetic Resonance* **238**, 94 (2014).
- [50] D. Yoon, M. Soundararajan, P. Cuanillon, F. Braunmueller, S. Alberti, and J.-P. Ansermet, *Journal of Magnetic Resonance* **262**, 62 (2016).
- [51] D. Shimon, Y. Hovav, A. Feintuch, D. Goldfarb, and S. Vega, *Physical Chemistry Chemical Physics* **14**, 5729 (2012).
- [52] L. R. Becerra, G. J. Gerfen, R. J. Temkin, D. J. Singel, and R. G. Griffin, *Physical Review Letters* **71**, 3561 (1993).
- [53] T. V. Can, M. A. Caporini, F. Mentink-Vigier, B. Corzilius, J. J. Walish, M. Rosay, W. E. Maas, M. Baldus, S. Vega, T. M. Swager, and R. G. Griffin, *The Journal of Chemical Physics* **141**, 064202 (2014).
- [54] N. M. Loening, M. Rosay, V. Weis, and R. G. Griffin, *Journal of the American Chemical Society* **124**, 8808 (2002).

Bibliography

- [55] M. J. Prandolini, V. P. Denysenkov, M. Gafurov, S. Lyubenova, B. Endeward, M. Bennati, and T. F. Prisner, *Applied Magnetic Resonance* **34**, 399 (2008).
- [56] M. Gafurov, V. Denysenkov, M. J. Prandolini, and T. F. Prisner, *Applied Magnetic Resonance* **43**, 119 (2012).
- [57] P. Neugebauer, J. G. Krummenacker, V. P. Denysenkov, G. Parigi, C. Luchinat, and T. F. Prisner, *Physical Chemistry Chemical Physics* **15**, 6049 (2013).
- [58] H. G. Beljers, L. van der Kint, and J. S. van Wieringen, *Physical Review* **95**, 1683 (1954).
- [59] R. Wind, M. Duijvestijn, C. van der Lugt, A. Manenschijn, and J. Vriend, *Progress in Nuclear Magnetic Resonance Spectroscopy* **17**, 33 (1985).
- [60] W. Müller-Warmuth and K. Meise-Gresch, *Advances in Magnetic and Optical Resonance* **11**, edited by J. S. Waugh, 1 (1983).
- [61] M. Florent, I. Kaminker, V. Nagarajan, and D. Goldfarb, *Journal of Magnetic Resonance* **210**, 192 (2011).
- [62] L. Tang, C. Tsai, W. W. Gerberich, L. Kruckeberg, and D. R. Kania, *Biomaterials* **16**, 483 (1995).
- [63] C. O. Bretschneider, Ü. Akbey, F. Aussenac, G. L. Olsen, A. Feintuch, H. Oschkinat, and L. Frydman, *ChemPhysChem* **17**, 2691 (2016).
- [64] S. Stoll and A. Schweiger, *Journal of Magnetic Resonance* **178**, 42 (2006).
- [65] K. M. Reddy, S. V. Manorama, and A. R. Reddy, *Materials Chemistry and Physics* **78**, 239 (2003).
- [66] L. Liu, H. Zhao, J. M. Andino, and Y. Li, *ACS Catalysis* **2**, 1817 (2012).
- [67] T. Ohno, K. Sarukawa, K. Tokieda, and M. Matsumura, *Journal of Catalysis* **203**, 82 (2001).
- [68] R. F. Howe and M. Grätzel, *Journal of Physical Chemistry* **91**, 3906 (1987).
- [69] D. M. Murphy and M. Chiesa, *Electron Paramagnetic Resonance* **21**, edited by B. C. Gilbert, 105 (2008).
- [70] Y. Nakaoka and Y. Nosaka, *Journal of Photochemistry and Photobiology A: Chemistry* **110**, 299 (1997).
- [71] H. Onoda and A. Matsukura, *Journal of Asian Ceramic Societies* **3**, 27 (2015).
- [72] K. Komaguchi, H. Nakano, A. Araki, and Y. Harima, *Chemical Physics Letters* **428**, 338 (2006).
- [73] V. I. Krinichnyi, *Synthetic Metals* **108**, 173 (2000).
- [74] A. A. Syed and M. K. Dinesan, *Talanta* **38**, 815 (1991).
- [75] D. Yoon, M. Soundararajan, and J.-P. Ansermet, *Solid State Nuclear Magnetic Resonance* **70**, 48 (2015).
- [76] V. Fleisher and I. Merkulov, in *Optical orientation*, Vol. 8, edited by F. Meier and B. Zakharchenya, *Modern Problems in Condensed Matter Sciences* (Elsevier, 1984), pp. 173–258.

- [77] C. A. Michal and R. Tycko, Phys. Rev. B **60**, 8672 (1999).
- [78] R. Tycko, Solid State Nuclear Magnetic Resonance **11**, 1 (1998).

Curriculum Vitae

Murari Soundararajan

Laboratoire de Physique des Matériaux Nanostructurés

École Polytechnique Fédérale de Lausanne

CH-1015 Lausanne, Switzerland

murari.ksr@gmail.com

Personal details

Date of birth	02 April 1990
Nationality	Indian

Education

2014-2018	PhD student at EPFL, Faculty of Basic Sciences, under the supervision of Prof Jean-Philippe Ansermet in the Laboratory of Nanostructured Materials, Institute of Physics
2012-2014	Master's studies at EPFL: MSc in Physics
2008-2012	Bachelor's studies at the Indian Institute of Technology Delhi, New Delhi, India: BTech in Engineering Physics
1996-2008	School under the ICSE board and High School under the ISC board at Vidya Niketan School, Bangalore, India

Skills

Languages	English and Tamil (native languages) Hindi (fluent) French (B1 level)
Software	MATLAB, LabVIEW, Solidworks, LaTeX, Origin, C++
Experimental techniques	Nuclear magnetic resonance Electron spin resonance Cryogenic and vacuum technology Electronics

Teaching experience

2014-2017 Teaching assistant for Bachelor's courses at EPFL
Autumn semesters: PHYS-100 (Mechanics)
Spring semesters: PHYS-105 (Thermodynamics)

Publications

- *High-field liquid-state Dynamic Nuclear Polarization in microliter samples*
D. Yoon, A. Dimitriadis, **M. Soundararajan**, C. Caspers, J. Genoud, S. Alberti, E. De Rijk, J.-Ph. Ansermet
Accepted for publication in Analytical Chemistry, 2018. DOI:10.1021/acs.analchem.7b04700
- *Dynamic nuclear polarization by frequency modulation of a tunable gyrotron of 260 GHz*
D. Yoon, **M. Soundararajan**, P. Cuanillon, F. Braunmüller, S. Alberti, J.-Ph. Ansermet
Journal of Magnetic Resonance vol. 262, p. 62-67, 2016.
- *500-fold enhancement of in situ ¹³C liquid state NMR using gyrotron-driven temperature-jump DNP*
D. Yoon, **M. Soundararajan**, C. Caspers, F. Braunmüller, J. Genoud, S. Albert, J.-Ph. Ansermet
Journal of Magnetic Resonance vol. 270, p. 142-146, 2016.
- *Field and frequency modulated sub-THz electron spin resonance spectrometer*
C. Caspers, P. da Silva, **M. Soundararajan**, M. A. Haider, J.-Ph. Ansermet
APL Photonics vol. 1, num. 2, p. 026101, 2016.
- *Nuclear polarization by optical pumping in InP:Fe above liquid nitrogen temperature*
D. Yoon, **M. Soundararajan**, J.-Ph. Ansermet
Solid State Nuclear Magnetic Resonance vol. 70, p. 48-52, 2015.
- *Opto-spintronics in InP using ferromagnetic tunnel spin filters*
C. Caspers, D. Yoon, **M. Soundararajan**, J.-Ph. Ansermet
New Journal of Physics vol. 17, p. 162401, 2015.

